Title
Three-dimensional Semiflexible Network with Transient Cross-links: A Finite Element Kinetic Monte Carlo Approach

Author
Shen, Lu

Publication Date
2018

Peer reviewed|Thesis/dissertation

UNIVERSITY OF CALIFORNIA

Los Angeles

Three-dimensional Semiflexible Network with Transient Cross-links: A Finite Element Kinetic Monte Carlo Approach

A dissertation submitted in partial satisfaction

of the requirements for the degree

Doctor of Philosophy in Chemistry

by

Lu Shen

2018

ABSTRACT OF THE DISSERTATION

Three-dimensional Semiflexible Network with Transient Cross-links:
A Finite Element Kinetic Monte Carlo Approach

by

Lu Shen
Doctor of Philosophy in Chemistry
University of California, Los Angeles, 2018
Professor Alexander Jacob Levine, Chair

Semiflexible biopolymer networks cross-linked by noncovalent bonds allow the networks topology to evolve over time and in response to applied stress. We developed a finite element kinetic Monte Carlo simulation approach, which allows cross-links to reorganize in a three-dimensional network, to explore the dynamics of semiflexible networks with transient cross-links. We will first discuss this simulation strategy, and then apply this tool to explore the following aspects of semiflexible networks: The natural bundle formation and the dynamics of bundle growth, especially in density and energy. The stress relaxation of networks with constrained filaments under affine strain field, and we find the linear shear elasticity of these networks mainly arises from the deformation change of the high-energy cross-links orientating in certain directions, and both the number and the elastic energy growth of these cross-links scales linearly with strain. We also find the strain energy dissipates exponentially through the strain-induced cross-link reorganization, and the cross-link configuration is trained during this process in a manner that tends to maintain the current strain on the filaments. Finally we conclude with proposals for new experiments to test these numerical results.

The dissertation of Lu Shen is approved.

William M Gelbart

Roberto Peccei

Alexander Jacob Levine, Committee Chair

University of California, Los Angeles

2018

To my parents and S. Z. ...

TABLE OF CONTENTS

LIST OF FIGURES

LIST OF TABLES

ACKNOWLEDGMENTS

First of all, I would like to thank my advisor, Alex Levine, for leading me forward persistently on the way of becoming a better scientist. Throughout these years, Alex acts as a perfect example to me of thinking critically, hypothesizing creatively and working diligently. At the second year of graduate school, I first met him and became his teaching assistant for the thermal dynamics class, and his inspiring lectures and humorous teaching style attracted me immediately. In one class, Alex related the underlying physics of a reversible process to the Fermi's golden rule, which had never crossed my mind before. Realizing this is how brilliant physicists think when they understand the concepts inside out, I decided to switch to his group for more theoretical science, and he was kind enough to accept me. Today, I start to realize how lucky I was four and half years ago to have the opportunity working with him, since he taught me not only the problem solving skills, but also the ability to discover and relate individual facts to a complete science story, which I will hold onto for the rest of my life. Alex also encouraged me to explore as many courses in physics as I could, to know more aspects of general physics rather than only focusing on one specific area, so that I had the chance to taste a tip of the iceberg of those fields that interested me most when I was young. Alex is also a good man and a kind friend, who taught me many philosophies of life besides science throughout these years.

I would also like to thank Sanjay Dharmavaram. Without his patient guidance in C++ coding and helpful advises on the project, never was I able to keep developing the simulation method and pushing on the research project. Those inspiring discussions with him kept me learning week by week, and those scenes of the exciting moments and frustrating occasions when we were siting together in front of the computer coding and debugging still come to me constantly.

Next, I would like to thank my first advisor in graduate school, Anastassia Alexandrova, who brought me onto the scientific research path at the first place. Anastassia is a great theorist in chemistry, and she led me to the microscopic world of chemical bond and molecule

level dynamics, providing me patient guidance and key insights in developing integrated methods to solve complex problems. Anastassia is also a generous scientist and a good friend, when knowing I wanted to switch groups, she showed absolute supports for letting me chase my interests, and for that I am eternally grateful. The every-year Christmas party at her place with old group mates and friends always makes me feel at home.

I would also like to thank my committee members, Heather Maynard, William Gelbart, and Roberto Peccei, not only for their supports as academic supervisors, but also for being mentors in science to me. Professor Peccei showed me the beauty of theories combining quantum mechanics and relativity when I was attending his quantum mechanics class. These things suddenly opened up a whole new world for me, and he gave me the courage and motivation to switch groups after the second year in graduate school, which is stressful for sure but worthwhile for sure. Helping Professor Gelbart teach his statistical mechanics class was the highlight of my teaching assistant experience at graduate school. One day, he demonstrated a macroscopic analogue of a biopolymer for us, his semiflexible black belt, which had a huge stretching stiffness but an almost zero bending modulus. Professor Maynard gave me a chance to look at the biopolymers from another perspective, experiments. The collaboration work on biopolymer-linked dimer first time allowed me to feel the pleasure when a theory suggested by us can explain the experimental results.

To all my friends at UCLA, especially my office mates Jonathan Kernes and Valentin Slepukhin, I am so lucky to meet you and you all will be remembered.

At the end, I would like to thank my fiancee, Siqi. We had been through all the difficulties of living alone across the pacific ocean for too long to remember until you made the sacrifices to reunite. Your love and support are the most important things to my success in graduate school, just like they are to many other things worthwhile in life. This work would not have been finished without you.

-L. S.

VITA

2008–2012 B.S. (Physics), Sichuan University, Chengdu, China.

2012–2018 Teaching Assistant, Department of Chemistry and Biochemistry, UCLA.

2012–2014 Research Assistant, Department of Chemistry and Biochemistry, UCLA. Under direction of Professor Anastassia Alexandrova.

2014 M.S. (Chemistry and Biochemistry), UCLA.

2014–2018 Research Assistant, Department of Chemistry and Biochemistry, UCLA. Under direction of Professor Alexander Levine.

2015–2018 Ph.D. Candidate, Department of Chemistry and Biochemistry, UCLA.

PUBLICATIONS

Lu Shen, Caitlin G. Decker, Heather D. Maynard and Alex J. Levine, *Calculating the mean time to capture for tethered ligands and its effect on the chemical equilibrium of bound ligand pairs*, Data in Brief, 2016, 8, 506515. Research article.

Caitlin G. Decker, Yu Wang, Samantha J. Paluck, Lu Shen, Joseph A. Loo, Alex J. Levine, Lloyd S. Miller and Heather D. Maynard, *Fibroblast growth factor 2 dimer with superagonist in vitro activity improves granulation tissue formation during wound healing*, Biomaterials, 2016, 81, 157-168. Research article.

Jonny Dadras, Lu Shen and Anastassia Alexandrova, Pt-Zn Clusters on MgO(100) and TiO2(110): *Dramatically Different Sintering Behavior*, J. Phys. Chem. C, 2015, 119 (11),

60476055. Research article.

Lu Shen, Jonny Dadras and Anastassia N. Alexandrova, *Pure and Zn-Doped Pt Clusters Go Flat and Upright on MgO(100)*, Phys. Chem. Chem. Phys., 2014, 16, 26436-26442. Research article.

CHAPTER 1

Introduction

1.1 Semiflexible Filaments Networks

Cytoskeletal networks are found in eukaryotic cells and these networks play a crucial role in cell mechanics. These networks are formed by biopolymers connected through cross-linking molecules. For instance, F-actins biopolymers can be cross-linked by filamin A (FLNa) molecules and form F-actin networks[1]. These cytoskeletal biopolymers are typically polymerized from globular monomers, and they have a diameter of order $10nm$, a length between 2 and $70\mu m$ (average length is around $15\mu m$) and a persistence length of order $20\mu m$[1][2][3]. These biopolymers are usually treated as semiflexible filaments, whose bending rigidities are large enough to overcome the entropic tendency of crumpling up into random coils[4][5]. The cross-linking of these semiflexible filaments by elastic protein molecules has topologically transformed them into a network of unique bulk and shear elastic responses[2][6][7][8][9][10].

Theoretically, there are two important transitions to distinguish a network from a filament solution: the conductivity transition and the rigidity percolation transition.

First, the conductivity transition: For a filament solution with a very low density of cross-links, which are treated as pinned point-constraints between filaments and are not allowed to rotate, the filaments will be in a fluid state of either isolated filaments or non-connected small filament bundles or clusters. "Fluid" here indicates the filaments or small filament clusters behave as individual non-interacting "solute" molecules, and there is no essential connections between remote parts of the filaments, therefore, the bulk and shear moduli of the system is zero. The conductivity transition occurs when an infinite small but system-wide connected filament cluster first exits and the shear modulus of the system becomes

non-zero, as a "solid" does. This definition, again, is based on the assumption that the cross-links are non-rotatable, which is a very strong constraint[11][12].

Second, the rigidity percolation transition: If the cross-links are treated as point pins between filaments but allowed to freely rotate, a barely connected cluster above the conductivity transition can response to shear by purely translating and rotating filaments, and the shear modulus becomes zero again. With freely rotatable cross-links, the rigidity percolation transition occurs when the configuration of the cluster provides enough extra constraints such that the translational and rotational motions of filaments will not be enough to balance the introduced stress, and the filaments must deform in ways of stretching/compressing or bending. In this case, the shear modulus of the system becomes non-zero even though the cross-links are rotatable[13][14][15][16][17]. Only above this rigidity percolation transition, will we have a well-defined filament network from a topological perspective, and the discussions of this dissertation will focus on these networks.

1.1.1 Permanently cross-linked networks

During the exploration of the mechanical properties of these semiflexible networks, in order to simplify the theoretical and numerical simulation approaches, theorists have made a simple assumption that the cross-links are quenched as either point pins or non-elastic rods between filaments, and only the translational and rotational motions of these permanent cross-links have to be considered. In other words, the cross-links are treated as non-elastic rivet-like constraints and the filaments can rotate freely around them. Therefore, in response to stress, the deformations in the network only contain the bending, stretching/compressing and twisting motions of the filaments[18].

Based on the permanent cross-link assumption, a variety of theoretical and numerical studies have been done on the shear moduli of these networks, especially when frequency-dependent shears are applied on the networks. The rubber plateau shear modulus, found by MacKintosh *et al.* using an affine deformation theory[19], scales as a power-law of the filament concentration c and bending rigidity κ: $G' \sim \kappa(\kappa/k_BT)^{2/5}c^{11/5}$ for an entangled

filament solution and $G' \sim \frac{\kappa^2}{k_B T} c^{5/2}$ for a densely cross-linked network[2]. Around the same time, Kroy and Frey discovered the dependence of the plateau modulus on the filaments concentration and bending modulus under a nonaffine deformation. They use a *wormlike chains* (WLC) model to describe the filaments in a permanently cross-linked network and predict $G' \sim \kappa c^2$ for filaments at the stiff limit and $G' \sim c^{5/3} \kappa^{1/3} (k_B T)^{2/3}$ for filaments at the soft limit[20].

Whether the deformation of the network is affine or nonaffine under shear became a question until early 2000s. In 2003, Levine *et al.* found two qualitatively distinct regimes characterized by affine or nonaffine deformations above the rigidity percolation transition, the crossover is determined by a length scale as a function of cross-link density. Their theory considers the bending and extension/compression deformations of the filaments and the degree of cross-linking[8], where they also use the assumption of permanent cross-links. Soon after that, they gave a more detailed discussion revealing the nonaffine regime is the filament-bending dominated while the affine regime is the filament-stretching/compressing dominated[9]. In 2007, Levine *et al.* generated a similar conclusion by applying a 2-D effective medium theory to a disordered semiflexible network[21], and they obtained a phase diagram of the affine and nonaffine regimes[21][22]. In 2011, Levine *et al.* showed from numerical simulations that adding small fraction of stiffer filaments to a nonaffine network leads to an increase in the elastic moduli, and the addition of stiffer filaments results in different effects on affinely and nonaffinely deformed networks: affine networks become more affine, while the nonaffinely deformed networks become more nonaffine[23].

Besides the frequency-independent plateau shear modulus discussed above, there are also power-law frequency-dependent regimes at both low and high frequencies [24][25][26]. The low-frequency behavior is related to the transient cross-linking dynamics[5][27][28], which will be discussed in details in Section 1.1.2. Now we only focus on the high-frequency regime, where the cross-links can be treated as permanent.

In the high-frequency regime (i.e. the short-time regime), the cross-links can be treated as permanent constraints, since the binding and unbinding of the cross-links cannot react fast enough to the highly-oscillating shear. It is still appropriate to use the permanently cross-

linked network model and discuss the behavior of shear modulus at high frequency. In 1998, Gittes *et al.* found the dynamic modulus scales with frequency as a power-law of $G(\omega) \sim \omega^{3/4}$ at high-frequencies[29], where they use a "chains subjected to constraints (cross-links)" model. Morse reaches an identical conclusion by employing an effective entanglement "tube model" to the filaments[30][31]. This frequency dependence was quantitatively confirmed experimentally by Koenderink *et al.* on an *in vitro* F-actin network in 2006[25]. In 2008, Ward *et al.* also got the same $\frac{3}{4}$ power-law frequency-dependence from the experiments on an actin filaments network cross-linked by α-actinin-4[32]. These theoretical predictions and experimental observations can be understood in terms that the high-frequency shear stretches out the thermally excited transverse undulations of the filaments, which makes the filaments less compliant and stiffer, and the shear modulus is contributed independently by filaments in this regime since the modulus does not depend on network parameters such as the entanglement length[10][29].

1.1.2 Networks with transient cross-links

The permanent cross-link assumption is well suited for explaining the high-frequency rheology of semiflexible networks, however, many real networks are typically constructed with filaments connected by transient cross-links through noncovalent interactions. Such highly dynamical cross-linking behavior, at both local and large scales, allows the topology of the network to evolve over time in response to applied stress, especially at low frequencies[27][32][33][34][35]. In general, at short time scales, the molecular-level binding/unbinding mechanism determines the transient nature of cross-links, which macroscopically evolves the network through a series of topology change at long time scales. The effects of transient cross-linking mainly include power-law low frequency rheology, energy dissipation through cross-link rupture, and mechano-memory effects.

First, the power-law low frequency rheology: In contrast to the high frequency regime, where the shear modulus of the network is contributed by individual filament, the transient cross-links play a much more significant role in the low frequency regime. Instead

of the $\frac{3}{4}$ power-law dependence of shear modulus on frequency, the power-law becomes $G(\omega) \sim \omega^{1/2}$ at low frequencies. This behavior has been widely observed both in numerical simulations[27][35] and experiments[32][33][34][36], and such rheology can be understood in terms of the collective orientational fluctuations and large-scale network rearrangements due to cross-link reorganization at a nonequilibrium state[27][28][35][37].

Second, the energy dissipation through cross-link rupture: In the shear modulus against frequency rheological spectrum of semiflexible networks, besides the high frequency $G(\omega) \sim \omega^{3/4}$ regime (for times much shorter than the cross-link lifetime) and the low frequency $G(\omega) \sim \omega^{1/2}$ regime (for times much longer than the cross-link lifetime), there is also a frequency-independent plateau modulus regime at intermediate frequencies (for times from 1 to 10^3 times of the cross-link lifetime). At the intermediate-frequency regime, the rheology of plateau modulus can be explained by the dissipative cross-link unbinding dynamics[27][28][35], where the stress-induced force on the cross-links leads to local bond rupture but without large-scale network rearrangements. An approach to study the cross-link breakage of these networks is the bead pulling experiment done by Valentine *et al.* in 2013[38]. They use a micro magnetic tweezer device to apply a force on a bead (of a much larger size of the network's mesh size) placed in the network, and try to pull it through the network. They observe a nonlinear response of the network at a short time scale and a significant bead jump at a time scale much longer than the cross-link lifetime. The nonlinear response of the network at a relatively short time scale can be explained by the force-induced unbinding events of the cross-links, and such cross-link rupturing events eventually lead to local network rearrangement. The significant bead jump is due to the breakage of old cross-links under load and the bead move to a new position where the force can be balanced. This bead pulling experiment is modeled by Levine *et al.* later in 2015[39] as single filament peeling from an array of cross-links, in which the cross-links unbinding mechanism is based on the Bell model[40] (Bell model will be discussed in Section 1.2.1). They found the cross-link breaking proceeds sequentially down the array from the point of loading in a series of energy-dissipative stochastic rupture events.

Third, the mechano-memory effects: The nonlinear elastic response of the transiently

cross-linked network to external shear also gives rise to the possibility of encoding mechano-memory in the network. Inspired by the fact that the mechanical response of semiflexible networks can be either reversible or irreversible under stress[10][41] and the network nematic order change under deformation[42][43], a mechano-memory due to static training shear can be accomplished. This mechano-memory is related to the change in nematic order parameter of the filaments, the training shear forces the network to rearrange in a way that the filaments tend to tilt along the stress. The training leads to an increase of the nematic order parameter and a rotation of the nematic director, and the network will have the "memory" to preserve the nematic order and director after training. This mechano-memory can also be erased by training in the opposite direction with the same amount of strain. This memory effect can be understood in term of the network's rearrangement of its transient cross-links under a strained deformation of filaments[44].

1.2 Cross-link Properties

As discussed in Section 1.1, the cross-links, which determine the topology of the network, are treated as freely-rotating rivet-like constraints of filaments in analytical studies, and only their statistical behavior is considered. However, real cross-links are also able to deform and store elastic energy. In this section we will enrich the elastic properties of cross-links from both physiological and modeling perspectives.

The cross-linking elastic protein molecules, such as FLNa or α-actinin-4, can form non-covalent bonds with one filament (i.e. F-actin) and branch out to attach another filament. In eukaryotic cells, the rest length of cross-links is of order $\sim 40nm$[6][7]. From a dynamics perspective, the cross-link can detach following Bell model unbinding mechanism[40], and there are two types of cross-links. The first type of cross-links is called "slip bond": when a tensile force is applied to the cross-link, it detaches more quickly due to a decreasing lifetime (or an increasing detaching rate) under load. The other type of cross-links is called "catch bond", and they response to applied force in an opposite way: their lifetime increases with an increasing tensile force[45][46][47]. We will discuss these two types of bonds and their

influence on networks under stress in details in Section 1.2.1.

1.2.1 Cross-link models: slip and catch bonds

The first type of cross-links is the slip bond, which is well understood and studied since Bell model is proposed in 1978[40]. As Bell showed in his work, the lifetime of a bond τ can be written in terms of $\tau = \tau^* \exp\left[(\varepsilon_b - \Gamma f)/k_B T\right]$, where τ^* is the reciprocal of a natural frequency of oscillation atoms in solid ($\sim 10^{-13} s$), ε_b is the chemical binding energy of the bond, f is the applied tensile force, and Γ is a parameter determined by the structure of bond molecule. In Bell's work, the potential energy of a slip bond is assumed harmonic-oscillator-like with a barrier. A stretching force on the bond drags the barrier down, therefore, decreases the lifetime of the bond[40]. A binding/unbinding mechanics based on Bell model is used in this dissertation, and will be discussed in details in Chapter 2.

In contrast to a slip bond, a catch bond is the type of non-covalent bond whose lifetime increases with tensile force applied to the bond before it reaches a maximum, and then decreases exponentially like a slip bond. This bond type is first proposed by Dembo *et al.* in 1998[45]. While studying the critical force needed to detach a adhesion molecules, they found some molecules bond more tightly under tension. In 2003, Marshall *et al.* also found the evidence of a catch bond when studying P-selectin glycoprotein ligand-1 (PSGL-1) bonds. They found an increasing force first prolongs the lifetime of PSGL-1 until it reaches a maximum and then starts to shorten its lifetime above the critical force[46]. A catch bond is also used to explain the leukocyte extravasation process. Shear stress induced by inflammation and hydrodynamic fluid causes leukocytes to bind with and roll on the endothelial vessel wall rather than float away[48]. The mechanism of the catch bond from a molecular level is not yet well understood, one explanation given by Sivasankar *et al.* in 2014 is that the force-induced and long-lived hydrogen bonds lock the non-covalent bond into tighter contact and prolong its lifetime[7][47]. Recently, an analytical model of catch-slip bond is also proposed based on a one-dimensional two-pathway free-energy potential well model by Bullerjahn and Kroy[49]. They find the mean lifetime of a virtual particle in

the two barrier potential increases first with an increasing load until it reaches a maximum, and then starts to decrease when passing the critical load.

Due to the different behaviors of catch and slip bonds, obviously a question may be asked: how will the catch bond affect the elasticity of our semiflexible networks? Interestingly, a number of experiments of networks with actin and myosin[50][51] or α-actinin-4[52] cross-links showed a counter intuitive response to stress. Since the detachment rate of catch bond decreases with an increasing stress, the upper bound of the cross-link governed regime shifts to lower frequencies with an increasing stress[5]. The increasing stress tightens the catch bonds and prolongs their lifetime, and the low-frequency regime will shift to even lower frequencies to provide long enough time for the network to rearrange through a reduced dynamics of cross-links reorganization.

1.3 Time Scales in the Model

Semiflexible networks respond to stress dramatically different at different time scales. In this section, multiple physical pictures will be discussed involving these large range of hierarchical time scales. This dissertation will specifically focus on the extremely long time scale (or zero-frequency regime).

The natural period of cross-link bond oscillation is of order $\sim 10^{-9}$ second[40], which is due to the oscillation of atoms in materials of order $\sim 10^{-13}$ second. Quantum chemistry dominates the microscopic mechanics and molecule-level dynamics in this time scale, which is the ultra-fast regime.

The typical cross-link lifetime time scale is of order $\tau \sim 10^{-3}$ second. The cross-link lifetime also determines the time scale of high-frequency rheology, where the frequency should be $> 1/\tau$. In the time scale one or two orders of magnitude shorter than the cross-link lifetime, the rheology is dominated by single-filament or single-bundle dynamics where the cross-links can by treated as permanent, as cross-links fail to break and reorganize the network in this time regime[25][35][53][54][55].

The long time scale, which is the low-frequency rheology regime, is of order minutes. The rheology is understood through large-scale network rearrangements due to cross-links reorganization[27][54].

There is also an intermediate time scale of order $10^{-3} \sim 1$ second, where the plateau modulus G' becomes frequency-independent, the rheology can be explained by the dissipative cross-link unbinding dynamics[27][28][35]

This dissertation will focus on the extremely low frequency regime, corresponding to the time scale of network stress relaxation involving large-scale filaments and cross-links rearrangement. In practice, a strain controlled step shear will be applied to the network, corresponding to a zero-frequency shear.

1.4 Outline of Text

In Chapter 2, we will discuss the numerical model employed in the simulation of semi-flexible networks in details, including the Kinetic Monte Carlo (KMC) method, the finite element treatment, and the Limited-memory Broyden-Fletcher-Goldfarb-Shanno (L-BFGS) algorithm. The KMC method is used to implement the transient nature of cross-links through a series of stochastic cross-link binding and unbinding events, where the probabilities of cross-linking events are determined by the rate constants related to the physical parameters of the cross-links. The finite element treatment allows us translating the original system of continuous filaments to a finite, discrete, and solvable numerical problem, where the filaments are considered as a collection of elemental segments of linear and angular springs. The L-BFGS algorithm is an iterative method for solving unconstrained nonlinear optimization problems, in this case, it minimizes the elastic energy and searches for the optimal configuration of the filaments when the topology of the network changes through cross-linking. The way we integrate these ideas and make it an available high-efficient tool for semiflexible network simulations will be introduced at the end of this chapter, providing a flow path of the "finite element Kinetic Monte Carlo" algorithm and two primary tests on the validity and precision of the KMC method and L-BFGS solver respectively.

In Chapter 3, we will apply the finite element Kinetic Monte Carlo approach to a three dimensional filament-constrained network with transient cross-links, and explore the dynamics of the cross-links during stress relaxation when a uniform strain field is applied to the network. We find the three dimensional network behaves as a linear shear elastic material under strain from both theoretical and numerical simulation approaches, where the strain energy mainly arises from the deformation growth of highly-stretched cross-links orientating in certain directions. We also observe the strain energy dissipation through strain-driven cross-link reorganization, where the stress relaxation can also be understood as a training process that results in an updated configuration of cross-links tending to maintain the strain field applied on the filaments.

In Chapter 4, we will explore the dynamics of the observed natural bundle formation of semiflexible networks in the presence of transient cross-links. We find the cross-linking dynamics is enhanced due to the catalysis of the cross-links themselves, which cumulatively results in a large number of slightly stretched intrabundle cross-links. We also discuss the bundling dynamics in the time-domain where the bundles grow rapidly, and we find the average (filament length) density and the average elastic energy density of the bundles both increase linearly over time, resulting in a conclusion that per unit length growth of the bundled filaments contributes a constant bundle elastic energy regardless of the time and the current density of the bundles. The bundle formation is a non-equilibrium process, and without setric interactions we speculate the network will eventually condense into a big bundle containing all filaments.

In the last chapter, we will summarize the main physical results of the dissertation surrounding the topic of semiflexible networks with transient cross-links. We will point out several directions to improve the current simulation method from different aspects. At the end, we will suggest possible experimental probes to verify the theories and simulation results in this work.

CHAPTER 2

Numerical Model

2.1 Introduction

In order to further explore the network formation and stress relaxation driven by stochastic cross-linking, a finite element kinetic Monte Carlo simulation approach is developed translating the originally continuous network to a discrete and finite problem that is numerically solvable. The microscopic cross-linking dynamics is achieved through a kinetic Monte Carlo (KMC) method[56][57][58][59], that determines which of the stochastic events of cross-link binding or unbinding to occur based on deformations of the cross-links. The idea of "finite element" is similar to the one used for Brownian dynamics simulations by Cyron *et al.*[60][61], in which filaments can be treated as a finite number of nodes and elemental segments of springs and angular springs, such that the filaments are allowed to store bending and stretching energies. Based on these structural set-ups, a Limited-memory Broyden-Fletcher-Goldfarb-Shanno algorithm (L-BFGS) algorithm is employed to minimize the total elastic energy of the network to search for the optimal network configuration when the network topology changes through cross-linking[62][63][64][65][66][67][68][69].

In this chapter, the rationales of KMC method, finite element treatment, and L-BFGS solver will be discussed in details. A general descriptions and further validations of the code, which successfully combines these ideas, will be provided at the end.

2.2 KMC Method

2.2.1 Cross-link binding and unbinding rates

The Kinetic Monte Carlo (KMC) method is used to simulate the microscopic binding and unbinding behaviors of cross-links based on the corresponding rates, which are determined by the deformation, the gas phase concentration, the chemical binding energy and the *thermal de Broglie wavelength* of the cross-links. The rates can be achieved from a statistical mechanics approach at equilibrium state: The free cross-links in our system can be treated as indistinguishable ideal gas particles. On the other hand, we consider the bound cross-links between filaments are at the condensed phase. When the system is at equilibrium, the temperature and chemical potential of these two coexisting phases should equal for all elastic energy level cross-links. This will result in a relation between the cross-linking rates and cross-link property parameters.

First, we can write down the ideal gas partition function of N indistinguishable cross-link particles in 3-D as

$$Z_N = \frac{1}{N!}\left(\int_V d^3\vec{r}\right)^N \left(\int d^3\vec{p}\; e^{\left[-\beta\vec{p}^2/2m\right]}\right)^N = \frac{1}{N!}\left(\frac{V}{\lambda_B^3}\right)^N, \tag{2.1}$$

where $\lambda_B = \frac{h}{(2\pi m k_B T)^{1/2}}$ is the *thermal de Broglie wavelength* of cross-links with mass m and at temperature T, h is the Planck constant and V is the volume of the system. The free energy of gas phase cross-links can be written as

$$\begin{aligned} F &= -k_B T \ln Z_N = k_B T \ln N! - k_B T N \ln\left(\frac{V}{\lambda_B^3}\right) \\ &\approx k_B T N \ln N - k_B T N + k_B T N \ln\left(\frac{\lambda_B^3}{V}\right) \\ &= k_B T N \ln\left(c\lambda_B^3\right) - k_B T N. \end{aligned} \tag{2.2}$$

Here we have used the Stirling's approximation $\ln N! \approx N \ln N - N$ for large N, and $c = N/V$ is the concentration of gas phase cross-links. Since the number of cross-links as free gas is much greater than the number of bound ones, we then assume this concentration is fixed during the entire cross-linking process. Therefore, the chemical potential of the gas phase

cross-links is determined by the concentration and the *thermal de Broglie wavelength* of cross-links

$$\mu = \left.\frac{\partial F}{\partial N}\right|_{T,V} = k_B T \ln\left(c\lambda_B^3\right). \tag{2.3}$$

Second, we consider the bound phase cross-links. Suppose each cross-link is a linear Hookean spring of stiffness k with a rest length a_c. At a separation x, the elastic deformation is $\Delta x = x - a_c$, and the total energy of a bound cross-link is

$$\varepsilon(x) = -\varepsilon_b + \epsilon_{CL}(\Delta x), \tag{2.4}$$

where ε_b is the chemical binding energy released when a cross-link is attached, $\epsilon_{CL}(\Delta x) = \frac{1}{2}k\Delta x^2$ is the elastic energy stored in a cross-link. Among all the N_S possible binding sites of an arbitrary separation x, if N_B of which are bound by cross-links, the partition function of "N_B-condensed" phase following Boltzmann distribution is then x dependent

$$Z_{N_B} = e^{-\beta N_B \varepsilon(x)} \binom{N_S}{N_B}, \tag{2.5}$$

the free energy of "N_B-condensed" phase can be written as

$$F_{N_B} = -k_B T \ln Z_{N_B} = -k_B T \left\{ -\beta N_B \varepsilon + \ln \binom{N_S}{N_B} \right\}. \tag{2.6}$$

We can again use Stirling's approximation to treat $\ln \binom{N_S}{N_B}$, assuming N_S and N_B are large.

$$\begin{aligned} \ln \binom{N_S}{N_B} =& \ln \left[\frac{N_S!}{N_B!(N_S - N_B)!} \right] \\ \approx& N_S \ln N_S - N_S - N_B \ln N_B + N_B \\ & - (N_S - N_B)\ln(N_S - N_B) + N_S - N_B \\ =& - N_S \left[z \ln z + (1-z)\ln(1-z) \right], \end{aligned} \tag{2.7}$$

where $z(x) = \frac{N_B(x)}{N_S(x)}$ is the binding fraction of cross-links with separation x. The free energy of "N_B-bound" phase is then

$$F_{N_B} = N_S \left\{ \varepsilon z + k_B T \left[z \ln z + (1-z)\ln(1-z) \right] \right\}, \tag{2.8}$$

and the chemical potential of this phase is

$$\mu_B = \left.\frac{\partial F_{N_B}}{\partial N_B}\right|_{T,N_S} = \left.\frac{\partial F_{N_B}}{\partial z}\right. \left.\frac{\partial z}{\partial N_B}\right|_{T,N_S} = \varepsilon + k_B T \ln\left(\frac{z(x)}{1 - z(x)}\right), \tag{2.9}$$

which just depends on the cross-link energy $\varepsilon(x)$, temperature T, and binding fraction $z(x)$.

Finally, we consider the contact equilibrium between the gas phase and the condensed phase of cross-links: the temperatures T and chemical potentials μ of cross-links at any separation x should be equal

$$\mu_B(x) = \mu = k_B T \ln\left(c\lambda_B^3\right). \tag{2.10}$$

This results in an equality of the binding fraction $z(x)$, gas phase cross-link concentration c, and the cross-link energy $\varepsilon(x)$ at separation x

$$\varepsilon(x) + k_B T \ln\left[\frac{z(x)}{1-z(x)}\right] = k_B T \ln\left(c\lambda_B^3\right). \tag{2.11}$$

Therefore, we have the binding ratio $z(x)$ as a function of c, T and Δx

$$\frac{N_B(x)}{N_S(x)} = z(x) = \frac{c\lambda_B^3 e^{-\frac{\varepsilon(x)}{k_B T}}}{1 + c\lambda_B^3 e^{-\frac{\varepsilon(x)}{k_B T}}} = \frac{c\lambda_B^3 e^{\frac{\varepsilon_b - \frac{1}{2}k\Delta x^2}{k_B T}}}{1 + c\lambda_B^3 e^{\frac{\varepsilon_b - \frac{1}{2}k\Delta x^2}{k_B T}}}. \tag{2.12}$$

From this equation, we can further derive the relationship between cross-link binding rate ν_{on} and unbinding rate ν_{off} for cross-link sites with separation x. When the system is at equilibrium, detailed balance requires

$$\nu_{on}(N_S - N_B) = \nu_{off} N_B. \tag{2.13}$$

The ratio of binding and unbinding rates of cross-links at an arbitrary separation x is

$$\frac{\nu_{on}(x)}{\nu_{off}(x)} = \frac{\frac{N_B(x)}{N_S(x)}}{1 - \frac{N_B(x)}{N_S(x)}} = c\lambda_B^3 e^{\frac{\varepsilon_b}{k_B T}} e^{-\frac{\frac{1}{2}k\Delta x^2}{k_B T}}. \tag{2.14}$$

Therefore, from this model, we immediately know the following: (i) The ratio of binding and unbinding rates only depends on four parameters: the gas phase cross-link concentration c and the *thermal de Broglie wavelength* $\lambda_B = \frac{h}{(2\pi m k_B T)^{1/2}}$ of cross-links, the chemical binding energy of two non-covalent bonds between both ends of the cross-link and corresponding filaments ε_b, and the possible-storing or already-stored elastic energy of the cross-link $\epsilon_{CL}(\Delta x) = \frac{1}{2}k\Delta x^2$. (ii) The binding and unbinding rates themselves should also depend on a mutual base rate of $\nu_0 \propto \frac{1}{\tau^*}$, where τ^* is a fundamental time scale related to the natural

period of bond oscillation as proposed in Bell model[40], so we can write binding rate ν_{on} and unbinding rate ν_{off} as

$$\begin{cases} \nu_{on} = & c\lambda_B^3 e^{\frac{\varepsilon_b}{k_B T}} \nu_0 e^{-\frac{\frac{1}{4}k\Delta x^2}{k_B T}} \\ \nu_{off} = & \nu_0 e^{\frac{\frac{1}{4}k\Delta x^2}{k_B T}} \end{cases} . \tag{2.15}$$

Here we have controlled the ratio of ν_{on} and ν_{off}, but the magnitude of rates also depends on a parameter ν_0, which should be inversely proportional to the average cross-linking event time. To normalize the affects of ν_0, we can take the time scale of average cross-link lifetime τ_0, instead of 'second', to serve as the time unit for system dynamics.

2.2.2 KMC algorithm

The basic algorithm of the KMC method based on the cross-linking rates contains three steps[56][57][58][59]: First, based on Equation 2.15, calculate the rate constants ν_{ij} of each possible cross-link binding or unbinding event that will lead the system from an initial state S_i to corresponding final state $S_{i,j}$ ($j = 1, 2, ..., N_k$), N_k is the total number of possible final states. The total rate of binding and unbinding over N_k possibilities is

$$\nu_{i,tot} = \sum_{j=1}^{N_k} \nu_{ij}. \tag{2.16}$$

Second, generate a uniform random number $\zeta_1 \in (0, 1]$, find l such that

$$\sum_{j=1}^{l-1} \nu_{ij} < \zeta_1 \nu_{i,tot} < \sum_{j=1}^{l} \nu_{ij}, \tag{2.17}$$

and then carry out the l-th cross-linking event that leads the system from S_i to the corresponding final state $S_{i,l}$. In this way, the probability of one binding or unbinding event to occur is proportional to its rate constant due to the uniform randomness of ζ_1. Third, advance the system time from initial state S_i to the stochastically selected final state $S_{i,l}$ by $\Delta t(i)$ drawn from the Poisson distribution described by the total rate $\nu_{i,tot}$. It is straightforward to know the probability that n cross-link binding or unbinding events occur during time interval dt is given by a Poisson distribution

$$P(n, dt) = \frac{e^{-\nu_{i,tot} dt} (\nu_{i,tot} dt)^n}{n!}. \tag{2.18}$$

Table 2.1: List of main symbols. Dimensions: $[L]$ =Length, $[t]$ =Time, $[F]$ =Force.

Symbol	Dimensions	Description
c	$[L]^{-3}$	Concentration of gas phase cross-links
a_c	$[L]$	Equilibrium length of cross-links
a_m	$[L]$	Maximum allowed length of cross-links
k	$[F][L]^{-1}$	Cross-link stretching stiffness
λ_B	$[L]$	*Thermal de Broglie wavelength* of cross-links
ε_b	$[F][L]$	Chemical binding energy of a cross-link
$\epsilon_{CL}(x)$	$[F][L]$	Elastic energy stored in a cross-link with length x
$z(x)$	1	Binding fraction of cross-links with length x
ν_{on}	$[t]^{-1}$	Cross-link binding rate
ν_{off}	$[t]^{-1}$	Cross-link unbinding rate
τ	$[t]$	Cross-links lifetime
N_{CL}	1	Total number of bound cross-links in the network
$\Delta t(i)$	$[t]$	Time interval of cross-linking event at i-th KMC iteration
k_T	$[F][L]^{-1}$	Effective (thermal) stretching stiffness of filament
a	$[L]$	Equilibrium length of filament segments
k_s	$[F][L]^{-1}$	Linear spring stiffness of filament segments
κ	$[F][L]^2$	Filament bending rigidity
κ_b	$[F][L]$	Angular spring stiffness of filament segments
ℓ	$[L]$	Filament equilibrium length
ℓ_p	$[L]$	Filament persistence length
γ	1	Strain
U	$[F][L]$	Strain energy
G	$[F][L]^{-2}$	Shear modulus
ξ	$[L]$	Mesh size

The time step $\Delta t(i)$ between two events at i-th KMC iteration can be characterized by the probability that zero cross-linking events has occurred during $\Delta t(i)$ as

$$P(0, \Delta t(i)) = e^{-\nu_{i,tot}\Delta t(i)}, \tag{2.19}$$

and this distribution of $\Delta t(i)$ leads to an average cross-linking event time at i-th KMC iteration as

$$< \Delta t(i) >= \frac{\int_0^\infty (\mathrm{d}t') e^{-\nu_{i,tot}t'} t'}{\int_0^\infty (\mathrm{d}t') e^{-\nu_{i,tot}t'}} = \frac{1}{\nu_{i,tot}}, \tag{2.20}$$

as expected. We can then generate another uniform random number $\zeta_2 \in (0, 1]$ representing the probability that zero cross-linking event occurs during $\Delta t(i)$, according to the distribution of $\Delta t(i)$ in Equation 2.19, the system time should be advanced by

$$\Delta t(i) = -\frac{\ln(\zeta_2)}{\nu_{i,tot}}. \tag{2.21}$$

Due to its "time-jumping" algorithm, we expect the KMC cross-linking method to be much more efficient than traditional Brownian dynamics simulations used to study filament networks with transient cross-links[35]. Its high efficiency can be attributed to skipping the very short time scales of bond oscillation motions or the smallest time steps needed in Brownian dynamics, and focusing on the time scales of stress relaxation. A physically occasional transition between network states cause by a cross-linking event is guaranteed to occur at each iteration step, rather than modeling the dynamics at every smallest time interval of the Brownian motion and waiting for a nontrivial event. KMC disregards the molecule-level dynamics and takes a much longer time scale of the network topology transition causing by cross-linking events. On the other hand, this time scale is fundamental for stress relaxation and network-scale cross-link reorganization, so that the resolution in the time measurement is fine enough to describe the stress relaxation.

2.3 Finite Element

The semiflexible network is modeled as a collection of N randomly oriented filaments and cross-links in a box with periodic boundary conditions applied in three dimensions. Each

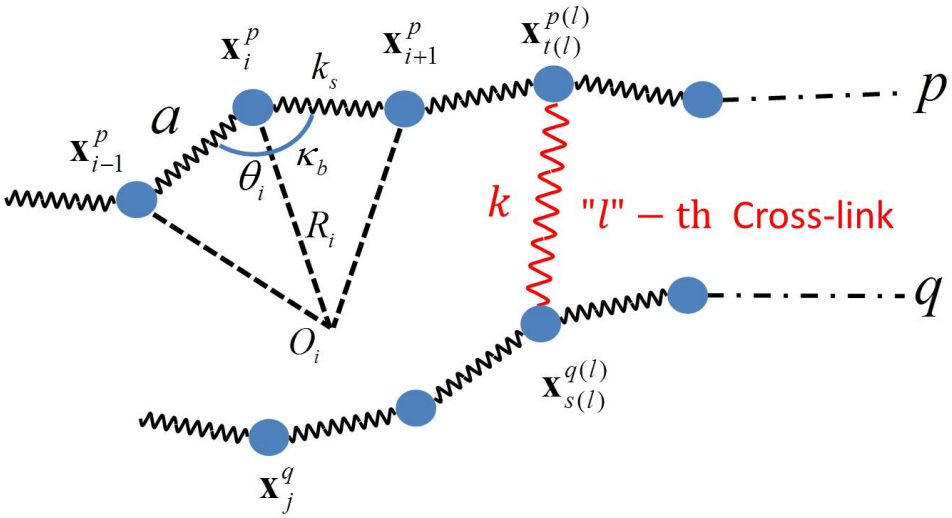

Figure 2.1: Schematic representation of the finite element method.

filament with an ID $p(p = 1, 2, ..., N)$ in the network is treated as a set of nodes with position $\mathbf{x}_i^p$ $(i = 1, 2, ..., n_f$, where n_f is the total number of nodes on a filament), as shown in Figure 2.1. The nodes on the same filament are connected in series by harmonic springs with stiffness k_s and a prescribed rest length a, which are used to model the stretching of the filaments. The nearest three nodes on the same filament also form an angular spring with stiffness κ_b, which accounts for the bending of the filaments. At an initial state without cross-links, the filaments are randomly distributed straight rods of length ℓ, the nodes on the same filament are now co-linear and are assumed evenly separated such that $a = \ell/(n_f - 1)$.

The bending energy carried by a semiflexible filament of length ℓ takes the form

$$E_{bend} = \frac{\kappa}{2} \int_0^\ell ds \left| \frac{\partial \vec{t}}{\partial s} \right|^2, \tag{2.22}$$

where κ is the bending modulus of the filament and $\vec{t}$ is the tangent vector along the filament, and the integrand represents the square of the local curvature along the filament. The filament position $\vec{r}(s)$ is now described by the arc-length coordinate s along the filament backbone. Therefore, the tangent vector is

$$\vec{t} = \frac{\partial \vec{r}}{\partial s}. \tag{2.23}$$

With the finite element treatment, the local curvature at node i on the filament can be approximated by the reciprocal of the radius $\frac{1}{R_i}$ of a circle that determined by nodes $i-1$, i,

and $i+1$ on the filament, as shown in Figure 2.1, the center of the circle is O_i and the local bending angle for the angular spring is $\pi - \theta_i$, where θ_i measures the angle between the two segments connecting node i ($\theta_i = \pi$ if the local bending is 0). Hence, the bending energy of the filament can be approximate as

$$E_{bend} \approx \frac{\kappa}{2} \sum_i \left(\frac{1}{R_i} \right)^2 a. \tag{2.24}$$

From the triangle of O_i, nodes i and $i-1$ (or $i+1$), the radius R_i and θ_i should follow the sine rule

$$\frac{a}{\sin(\pi - \theta_i)} = \frac{R_i}{\sin(\frac{\theta_i}{2})}, \tag{2.25}$$

which leads to

$$\frac{1}{R_i} = \frac{2}{a} \cos\left(\frac{\theta_i}{2} \right). \tag{2.26}$$

Therefore, the bending energy of the filament then can be written as

$$E_{bend} \approx \sum_i \frac{\kappa}{a} \left(1 + \cos\theta_i\right), \tag{2.27}$$

the term $\frac{\kappa}{a}\left(1 + \cos\theta_i\right)$ is the bending energy of node i on the filament, which is equivalent to the elastic energy of an effective angular spring with angular deformation of $(1 + \cos\theta_i)$ and stiffness of κ_b. The angular spring stiffness κ_b is equal to the ratio of filament bending modulus $\kappa = k_B T \ell_p$ and the rest length of filament segments a as

$$\kappa_b = \frac{\kappa}{a} = \frac{k_B T \ell_p (n_f - 1)}{\ell}, \tag{2.28}$$

where ℓ_p is the persistence length of the filament, ℓ is the equilibrium length of the filament, and k_B is the Boltzmann constant.

The effective (thermal) stretching stiffness k_T arising from the bending fluctuations of the semiflexible filaments can be written in terms as[5]

$$k_T = \frac{\kappa \ell_p}{\ell^4} = \frac{k_B T {\ell_p}^2}{\ell^4}. \tag{2.29}$$

Now we view the filament stretching from a finite element perspective, the filament is a series of $n_f - 1$ harmonic springs with an overall spring constant k_T. Hence, the effective spring constant k_s between two nearest nodes on a filament should be $n_f - 1$ times greater than k_T

$$k_s = (n_f - 1) k_T = \frac{k_B T {\ell_p}^2}{\ell^4} (n_f - 1). \tag{2.30}$$

Under the finite element treatment, the total elastic energy of the filaments now can be expressed as the sum of the deformation energies of local linear and angular springs

$$E_{fil} = \sum_{p=1}^{N} \sum_{i=1}^{n_f-1} \frac{k_s}{2} \left(|\mathbf{x}_i^p - \mathbf{x}_{i+1}^p| - a \right)^2 + \sum_{p=1}^{N} \sum_{i=2}^{n_f-1} \kappa_b \left(1 + \cos \theta_i^p \right), \tag{2.31}$$

where $\mathbf{x}_i^p$ is the position of i-th node on p-th filament, and θ_i^p is the angle between two segments connecting i-th node on p-th filament. With the finite element method, the elastic energy of the filaments can be approximate by a simple summation form instead of the original integration form, which dramatically simplifies the numerical calculation.

As discussed in Section 2.2, the cross-links that dynamically construct filaments into a network are treated as linear springs (with stiffness k and rest length a_c) that are allowed to connect a pair of nodes from filaments if the separation of the nodes is within a maximum allowed length of the cross-link. Each node on a filament can only be attached to one cross-link due to the biological structure of related chemical binding groups[2][6][7], and the cross-linking between nodes on the same filament is also forbidden in the simulation. Under these conditions, all the cross-linking rate constants at any given state of the network can be calculated providing the coordinates of the nodes, therefore, the finite element method also ensures the numerical feasibility of the KMC method for cross-linking by making the number of possible binding sites finite.

The total elastic energy stored in the cross-links now can also be expressed in terms of node positions as

$$E_{CL} = \sum_{l=1}^{N_{CL}} \frac{k}{2} \Big(|\mathbf{x}_{t(l)}^{p(l)} - \mathbf{x}_{s(l)}^{q(l)}| - a_c \Big)^2, \tag{2.32}$$

where N_{CL} is the total number of bound cross-links, $p(l)$ and $q(l)$ are the filaments that l-th cross-link connects through nodes $t(l)$ and $s(l)$ respectively, as shown in Figure 2.1.

The total elastic energy of the network $E_{el} = E_{fil} + E_{CL}$ and the total energy of the system $E_{tot} = E_{el} - \varepsilon_b N_{CL}$ at a given network configuration can both be numerically calculated through the finite element method. The accuracy of the method increases as the number of nodes on a filament n_f increases, as expected, the filaments resume continuous at $n_f \to \infty$ limit.

2.4 Numerical Solver: L-BFGS Algorithm

The topology of the network changes at times involving cross-link binding or unbinding events, where the filament nodes move due to unbalanced forces until the network reaches a new elastic equilibrium state. We use a quasi-Newton Limited-memory Broyden-Fletcher-Goldfarb-Shanno (L-BFGS) algorithm to find the optimal configuration of the network at the new elastic equilibrium state, through iteratively minimizing the elastic energy of the network[62][63][64][65][66][67][68][69].

Suppose the total elastic energy of the network E_{el} is the function $f(\mathbf{x})$ to minimize in this optimization problem, where $\mathbf{x}$ is a column vector of length $3Nn_f$ representing the set of all coordinate variables of the nodes in the network. There is no constraints on the values of $\mathbf{x}$, and f now is a differentiable scalar function.

The BFGS algorithm begins at an initial estimate for the optimal value $\mathbf{x}_0$ and proceeds iteratively for a better estimation of $\mathbf{x}_i$ at each step i. The second-order approximation of $f(\mathbf{x}_i)$ around an iterate at i-th step can be found by Taylor expanding the function in this high dimensional variable space to the second order

$$f(\mathbf{x}_i + \Delta\mathbf{x}) \approx f(\mathbf{x}_i) + \nabla f(\mathbf{x}_i)^{\mathrm{T}}\Delta\mathbf{x} + \frac{1}{2}\Delta\mathbf{x}^{\mathrm{T}}\boldsymbol{B}_i\Delta\mathbf{x}, \tag{2.33}$$

where ∇f is the gradient, and $\boldsymbol{B}_i$ is an approximation to the Hessian matrix at i-th step, which should be updated iteratively at each step. The gradient of the approximation with respect to $\Delta\mathbf{x}$ is then

$$\nabla f(\mathbf{x}_i + \Delta\mathbf{x}) \approx \nabla f(\mathbf{x}_i) + \boldsymbol{B}_i\Delta\mathbf{x}. \tag{2.34}$$

Ideally, we want to pick a $\Delta\mathbf{x}$ such that $\mathbf{x}_i + \Delta\mathbf{x}$ is a stationary point of f by setting the left hand side of the equation equal to zero. The BFGS algorithm is modified to include a small step size δ_i on the search direction $\mathbf{p}_i = \Delta\mathbf{x}$ provided by the analogue of the Newton equation at i-th step

$$\mathbf{p}_i = -\boldsymbol{B}_i^{-1}\nabla f(\mathbf{x}_i). \tag{2.35}$$

A linear search along the $\mathbf{p}_i$ direction is then performed to find the optimized step size δ_i

determined by the minimum of f along this direction such that

$$\delta_i = \arg\min f(\mathbf{x}_i + \delta_i \mathbf{p}_i). \tag{2.36}$$

The variation vector of node coordinates at step i is then chosen as $\mathbf{s}_i = \delta_i \mathbf{p}_i$ and the node coordinates of the step $i+1$ is updated by $\mathbf{x}_{i+1} = \mathbf{x}_i + \mathbf{s}_i$. The secant equation (the Taylor series of the gradient itself) can then be achieved from the quasi-Newton condition imposed on the update of $\boldsymbol{B}_i$ as

$$\boldsymbol{B}_{i+1}\mathbf{s}_i = \mathbf{y}_i, \tag{2.37}$$

where $\mathbf{y}_i = \nabla f(\mathbf{x}_{i+1}) - \nabla f(\mathbf{x}_i)$ is the gradient variation vector and $\mathbf{s}_i = \mathbf{x}_{i+1} - \mathbf{x}_i$ the node coordinates variation vector.

Instead of calculating the full Hessian matrix at new point $\mathbf{x}_{i+1}$ in the high dimensional variable space, an approximate Hessian can be iterated at step i by the addition of two symmetric rank-one matrices (SR1 method) while maintaining the symmetry and positive definiteness of $\boldsymbol{B}_{i+1}$

$$\boldsymbol{B}_{i+1} = \boldsymbol{B}_i + \alpha_i \mathbf{u}_i \mathbf{u}_i^{\mathrm{T}} + \beta_i \mathbf{v}_i \mathbf{v}_i^{\mathrm{T}}. \tag{2.38}$$

If choosing $\mathbf{u}_i = \mathbf{y}_i$ and $\mathbf{v}_i = \boldsymbol{B}_i \mathbf{s}_i$, the secant equation $\boldsymbol{B}_{i+1}\mathbf{s}_i = \mathbf{y}_i$ requires

$$\boldsymbol{B}_i \mathbf{s}_i + \alpha_i \mathbf{y}_i \mathbf{y}_i^{\mathrm{T}} \mathbf{s}_i + \beta_i \boldsymbol{B}_i \mathbf{s}_i \left(\mathbf{s}_i^{\mathrm{T}} \boldsymbol{B}_i \mathbf{s}_i\right) = \mathbf{y}_i, \tag{2.39}$$

which leads to the value of α_i and β_i as

$$\begin{cases} \alpha_i = & \frac{1}{\mathbf{y}_i^{\mathrm{T}} \mathbf{s}_i} \\ \beta_i = & -\frac{1}{\mathbf{s}_i^{\mathrm{T}} \boldsymbol{B}_i \mathbf{s}_i} \end{cases}. \tag{2.40}$$

By substituting α_i and β_i into Equation 2.38, the iterative equation of the approximate Hessian matrices can be expressed as

$$\boldsymbol{B}_{i+1} = \boldsymbol{B}_i + \frac{\mathbf{y}_i \mathbf{y}_i^{\mathrm{T}}}{\mathbf{y}_i^{\mathrm{T}} \mathbf{s}_i} - \frac{\boldsymbol{B}_i \mathbf{s}_i \mathbf{s}_i^{\mathrm{T}} \boldsymbol{B}_i}{\mathbf{s}_i^{\mathrm{T}} \boldsymbol{B}_i \mathbf{s}_i}. \tag{2.41}$$

The inverse of approximate Hessian matrix used to solve Equation 2.35 can be obtained by applying the Sherman-Morrison formula to $\boldsymbol{B}_{i+1}$ as[70]

$$\boldsymbol{B}_{i+1}^{-1} = \left(I - \frac{\mathbf{s}_i \mathbf{y}_i^{\mathrm{T}}}{\mathbf{y}_i^{\mathrm{T}} \mathbf{s}_i}\right) \boldsymbol{B}_i^{-1} \left(I - \frac{\mathbf{y}_i \mathbf{s}_i^{\mathrm{T}}}{\mathbf{y}_i^{\mathrm{T}} \mathbf{s}_i}\right) + \frac{\mathbf{s}_i \mathbf{s}_i^{\mathrm{T}}}{\mathbf{y}_i^{\mathrm{T}} \mathbf{s}_i}. \tag{2.42}$$

To improve the computational efficiency, realizing that $\boldsymbol{B}_i^{-1}$ is symmetric and that $\mathbf{y}_i^{\mathrm{T}}\boldsymbol{B}_i^{-1}\mathbf{y}_i$ and $\mathbf{y}_i^{\mathrm{T}}\mathbf{s}_i$ are both scalars, this iteration of $\boldsymbol{B}_i^{-1}$ can be written in a form without temporary matrices as

$$\boldsymbol{B}_{i+1}^{-1} = \boldsymbol{B}_i^{-1} + \frac{(\mathbf{y}_i^{\mathrm{T}}\mathbf{s}_i + \mathbf{y}_i^{\mathrm{T}}\boldsymbol{B}_i^{-1}\mathbf{y}_i)}{(\mathbf{y}_i^{\mathrm{T}}\mathbf{s}_i)^2}\mathbf{s}_i\mathbf{s}_i^{\mathrm{T}} - \frac{1}{\mathbf{y}_i^{\mathrm{T}}\mathbf{s}_i}(\boldsymbol{B}_i^{-1}\mathbf{y}_i\mathbf{s}_i^{\mathrm{T}} + \mathbf{s}_i\mathbf{y}_i^{\mathrm{T}}\boldsymbol{B}_i^{-1}). \tag{2.43}$$

In practice, the first approximate Hessian matrix $\boldsymbol{B}_0$ can be chosen as the identity matrix $\boldsymbol{I}$, and $\boldsymbol{B}_i$ will be refined during the iteration while the coordinate vector of filament nodes $\mathbf{x}_i$ is optimized synchronously. The convergence at step i can be checked by evaluating the norm of gradient $||\nabla f(\mathbf{x}_i)||$, therefore, it is straightforward to propose an adjustable parameter of a small number g_0 representing the optimization precision, which signals the solver to stop further iterations as long as $||\nabla f(\mathbf{x}_i)|| < g_0$. A reasonable choice of g_0 based on the network parameters can dramatically save the computational resource and time, while still provides considerably good optimizations.

The main disadvantage of BFGS algorithm is need to store the approximation Hessian matrices $\boldsymbol{B}_i$ or the inverse Hessian matrices $\boldsymbol{B}_i^{-1}$, where the computational storage required scales quadratically with the number of variables (nodes) in the system as $\sim (Nn_f)^2$. To minimize the usage of computer memory, a Limited-memory version of BFGS (L-BFGS) algorithm is used instead in this dissertation[66][67][68][69]. The rationale of L-BFGS algorithm is the same as BFGS, however, it only stores a few vectors that represent $\boldsymbol{B}_i$ or $\boldsymbol{B}_i^{-1}$ implicitly by maintaining the history of a small number n_L (often $n_L < 10$) of the most recent coordinate variation vectors $\mathbf{s}_i$ and gradient variation vectors $\mathbf{y}_i$. The approximate inverse Hessian matrices $\boldsymbol{B}_j^{-1}$ is evaluated recursively using Equation 2.43 (for $i = j-1, j-2, ..., j-n_L$) form the stored variational vectors and a prescribed "initial" approximation of the inverse Hessian at the oldest stored step (e.g. $\boldsymbol{B}_{j-n_L}^{-1} = I$). Therefore, with this "limited-memory" modification, the computational storage required for L-BFGS algorithm scales linearly with the number of variables (nodes) in the system as $\sim Nn_f$, instead of the quadratic scaling for BFGS algorithm. Due to this linear computer memory requirement, the L-BFGS method is particularly well suited for optimization problems with a large number of variables, such as our semiflexible network under the finite element treatment.

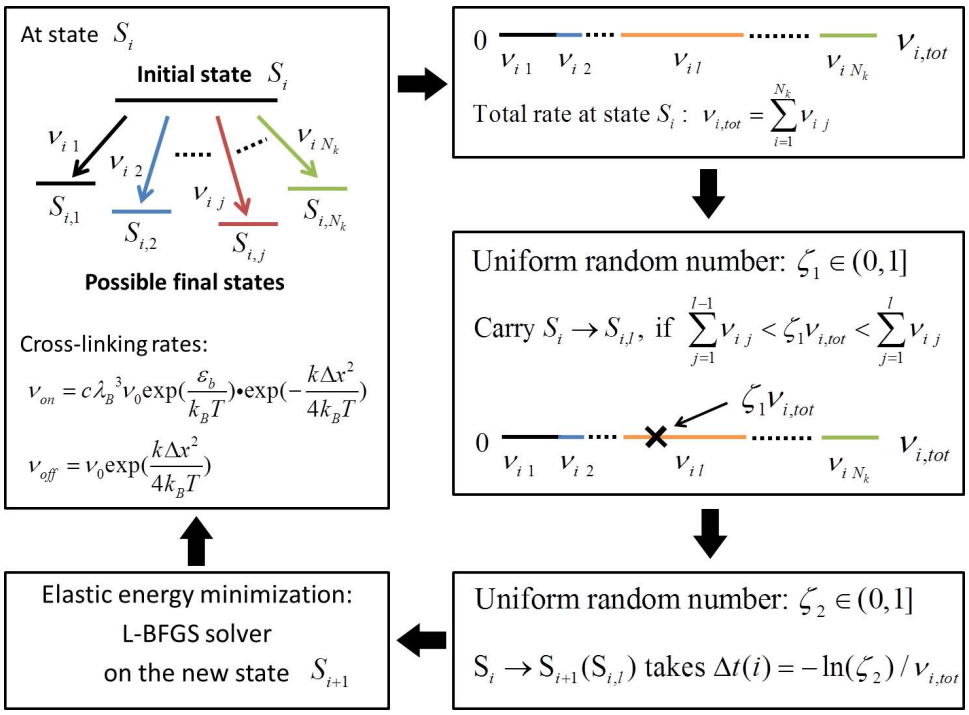

Figure 2.2: Flowchart of the finite element kinetic Monte Carlo algorithm.

2.5 Description and Validation of the Code

The dynamics of cross-links and filaments in the network can be numerically modeled by integrating the individual code of KMC method and L-BFGS solver under the finite element treatment, where the part of KMC method realizes the dynamical cross-linking that triggers the topology change of the network and the part of L-BFGS solver seeks for the new elastic equilibrium and updates the network configuration. This combined tool has been implemented as a part of VOOM v.2 (Variational Object-Oriented Mechanics) package, an open source library developed by Klug, et. al and published under the MIT license[71]. The library is a collection of C++ classes designed for the numerical simulations of continuum solid, structural mechanics and biophysics problems. In this section, a general description of the code working principle and two basic validations of the code on simple systems will be discussed.

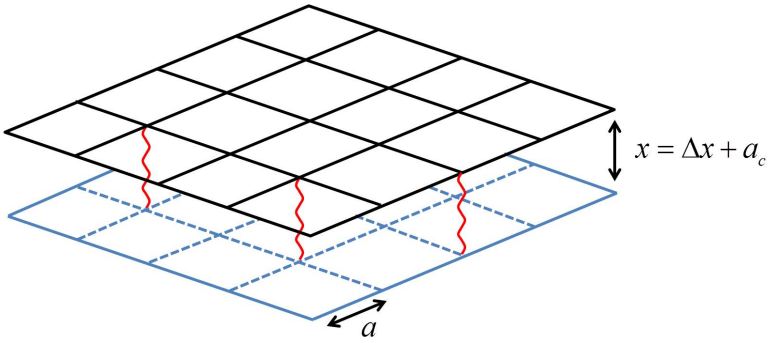

Figure 2.3: Schematic framework of the Boltzmann distribution test. The aligned top (black) and bottom (blue) lattices are both constructed by N^2 ($N = 100$) orthogonal filaments intersecting at their nodes. The lattice constant is equal to the equilibrium length of filament segments a, and the separation of the two layers is the variable x. The filament nodes are strictly constrained in space, and we only allow the formation and breakage of vertical cross-links between aligned node pairs (red), resulting in an identical deformation for all potential cross-links (at a specific separation x) and a fixed number of possible binding sites $N_S = 10000$ (for any separation x).

2.5.1 Finite element KMC algorithm flow path

The working process of the finite element KMC algorithm used in this dissertation is shown as the flowchart in Figure 2.2. At a given state S_i, the code first evaluates the unbinding rate constants of all bound cross-links and the possible binding rate constants of all candidate node pairs based on the current coordinates of the filament nodes and Equation 2.15. When computing the binding rates, it is not necessary to consider all nodes pairs in the entire network, instead, the code is able to select the local node pairs within a maximum allowed cross-link length. The potential cross-linking of nodes on the same filament is also excluded in this step. Second, the code randomly selects one of the cross-linking event to carry out according to the probabilities proportional to their rate constants, which represents the stochastic nature of cross-linking and leads the network form state S_i to state S_{i+1}. Third, the code computes the time of the selected cross-linking event by drawing the lifetime of state S_i from a Poisson distribution described by the total rate constant $\nu_{i,tot}$ at this state. Finally,

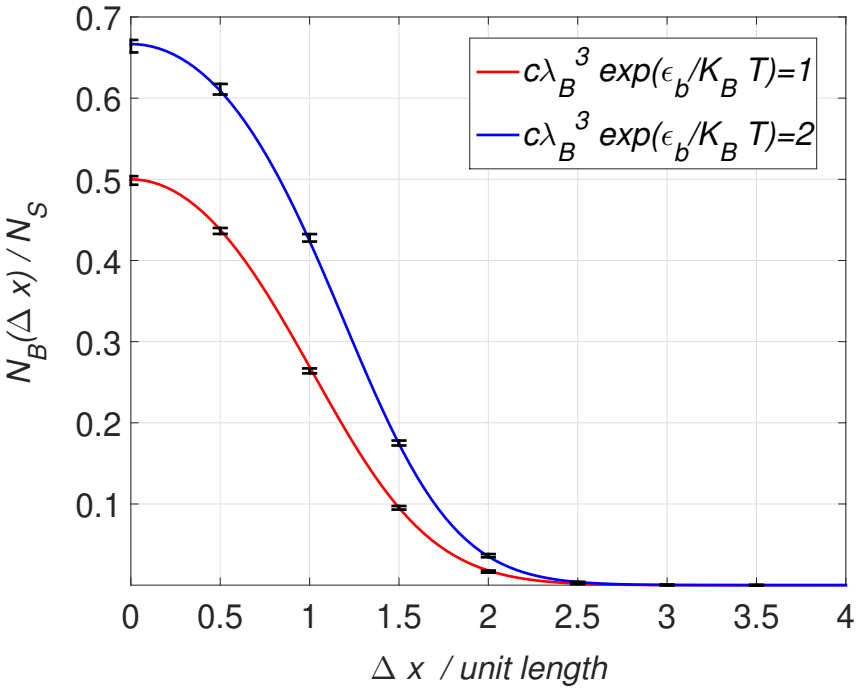

Figure 2.4: Test of Boltzmann distribution of cross-link energy. Cross-link binding fraction $N_B(\Delta x)/N_S$ against cross-link deformation Δx measured in *unit length*, with theoretical prediction curves of $c\lambda_B^3 e^{\frac{\varepsilon_b}{k_B T}} = 1$ (red), $c\lambda_B^3 e^{\frac{\varepsilon_b}{k_B T}} = 2$ (blue), and simulation data points (black) with error bars. The cross-link stretching stiffness is set to be $\frac{2k_B T}{(unit\ length)^2}$ for simplicity.

the L-BFGS solver is launched searching for the optimized configuration of the network for S_{i+1} state, which will serve as the initial state for the next cycle. The time spent from the moment of cross-linking till the moment that the network regains elastic equilibrium is ignored, since the L-BFGS solving algorithm is physical time irrelevant.

2.5.2 Boltzmann distribution test

The physical validity of KMC cross-linking method can be checked through a simple Boltzmann distribution test on the framework of two-layer aligned lattices of constrained filaments, as shown in Figure 2.3. In the test, each lattice layer contains N (e.g. =100) "East-West" and N "North-South" strictly constrained filaments intersecting at their nodes with a lattice

constant a equal to the rest length of filament segments, and the two layers are perfectly aligned with a controlled separation x satisfying the condition of $a_c \leq x \ll a$, where a_c is the equilibrium length of cross-links. The maximum search radius of potential cross-links R_s follows the condition of $x < R_s < a$, such that the cross-links can only form vertically between aligned node pairs, resulting in an identical deformation for all potential cross-links (at a specific separation x) and a fixed number of possible binding sites $N_s = N^2$ (for any separation x).

The test is performed by varying the separation x and checking how the binding fraction of cross-links change as a function of cross-link deformation. If the cross-links energy $\varepsilon(\Delta x) = -\varepsilon_b + \frac{1}{2}k\Delta x^2$ with deformation $\Delta x = x - a_c$ follows the Boltzmann distribution, the binding fraction $\frac{N_B(\Delta x)}{N_S}$ should follow Equation 2.12. In this two-layer constrained lattices case, with a constant N_S for all Δx, we should have

$$\frac{N_B(\Delta x)}{N_S} = \frac{c\lambda_B^3 e^{\frac{\varepsilon_b}{k_B T}} e^{\frac{-k\Delta x^2}{2k_B T}}}{1 + c\lambda_B^3 e^{\frac{\varepsilon_b}{k_B T}} e^{\frac{-k\Delta x^2}{2k_B T}}}, \tag{2.44}$$

where the number of bound cross-links $N_B(\Delta x)$ can be acquired through this test model by simply counting the number of cross-linked node pairs after it reaches equilibrium at separation $x = \Delta x + a_c$.

To simplify the test, the gas phase cross-link concentration c, the *thermal de Broglie wavelength* λ_B, and the chemical binding energy ε_b of cross-links are set such that $c\lambda_B^3 e^{\frac{\varepsilon_b}{k_B T}} = 1$ (or 2). The deformation of cross-links Δx is measured in *unit length*, and the cross-link stretching stiffness k is set to be $\frac{2k_B T}{(unit\ length)^2}$.

The test results are shown in Figure 2.4, where the black points with error bars are the binding fractions acquired from the simulation and the red (blue) curve is the theoretical prediction with $c\lambda_B^3 e^{\frac{\varepsilon_b}{k_B T}} = 1\ (= 2)$ and $k = \frac{2k_B T}{(unit\ length)^2}$. As expected, the simulation results agree with the theoretical predictions of Equation 2.44, confirming the basic physical validity of KMC method during the highly-efficient stochastic cross-linking process. In addition, the binding fraction at a given deformation is a monotonic increasing function of the gas phase cross-link concentration c, since the first order derivative of Equation 2.44 with respect to c at a fixed Δx is always positive. This fact can be understood in terms of the Le Chatelier's

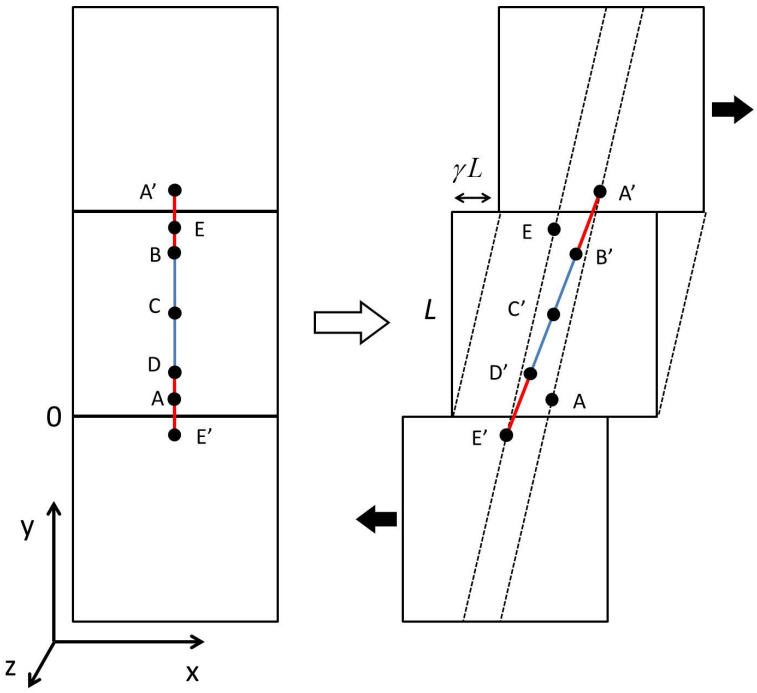

Figure 2.5: Shear through Lees-Edwards boundary conditions and single filament test framework (projected view on x-y plane). The unit cells are perfectly aligned in an unstrained case (left), a strain γ in +x direction is applied (right) by adding constant offsets of γL and $-\gamma L$ to the top and bottom unit cells. This operation is equivalent to re-setting the unit cell as a parallelepiped instead of a cube, node A (E) will be mapped to A' (E') in the top (bottom) unit cell with an offset of γL ($-\gamma L$) in x coordinates (right figure). A filament (blue segments) of three free nodes B C D is placed in the center of the unit cell perpendicular to x-z plane in an unstrained state (left figure), with terminal node B (D) cross-linked to constrained nodes A (E) through the top (bottom) face of the center unit cell. The cross-links are shown as red segments between node B (D) and virtual node A' (E') of physical node A (B). In a strain state (right figure), the filament nodes move to new positions at B' C' D', such that the system reaches the elastic equilibrium, where A' B' C' D' E' are co-linear and |A'B'|=|B'C'|=|C'D'|=|D'E'| if $a = a_c$ and $k_s = k$.

principle, where the shifting of equilibrium tends to cancel the increasing number of gas phase cross-links by forming more condensed ones.

2.5.3 Strain controlled shear and single filament test

The strain controlled shear is applied to the network through Lees-Edwards boundary conditions by adding a constant horizontal offset to filaments and cross-links that cross the top and bottom boundaries[72]. In the simulation, since filaments are considered as a collection of nodes in a box with periodic boundary conditions, the shear can be interpreted as a shift of the periodic boundaries, where the unit cell changes shape from a cube to a parallelepiped, as shown in Figure 2.5. Node A (E) is mapped to a virtual node A' (E') in the top (bottom) unit cell and the x coordinates of A and A' (E and E') are identical in an unstrained case (Figure 2.5, left), while in a strained case (Figure 2.5, right), their x coordinates differ by γL ($-\gamma L$) if γ is the strain and L is edge length of an unstrained unit cell.

A simple test on the performance of L-BFGS solver can be implemented by comparing the configuration and elastic energy of a sheared single filament system to the theoretical predictions. At an unstrained state, the filament of three nodes and length $\ell = 0.6L$ (with an equilibrium length of filament segment $a = 0.3L$) is placed in the center of the unit cell perpendicularly to x-z plane, shown as the blue segments in Figure 2.5 (left), and the coordinates of the filament nodes are: B $(0.5L, 0.8L, 0.5L)$, C $(0.5L, 0.5L, 0.5L)$, and D $(0.5L, 0.2L, 0.5L)$. There are also two constrained individual nodes A $(0.5L, 0.1L, 0.5L)$ and E $(0.5L, 0.9L, 0.5L)$ in the unit cell with their virtual nodes A' $(0.5L, 1.1L, 0.5L)$ and E' $(0.5L, -0.1L, 0.5L)$ mapped into the top and bottom unit cells, respectively. Node A (E) is cross-linked with node B (D) through the top (bottom) face of the center unit cell, which is equivalent to the cross-linking between virtual node A' (E') and node B (D), shown as the red segments in Figure 2.5 (left), where the cross-links are assumed having a same equilibrium length with filament segments ($a_c = a = 0.3L$) and they are un-stretched at this state.

When a strain γ is applied to the system through Lees-Edwards boundary conditions, the virtual node A' (E') in the top (bottom) unit cell should carry a displacement of γL

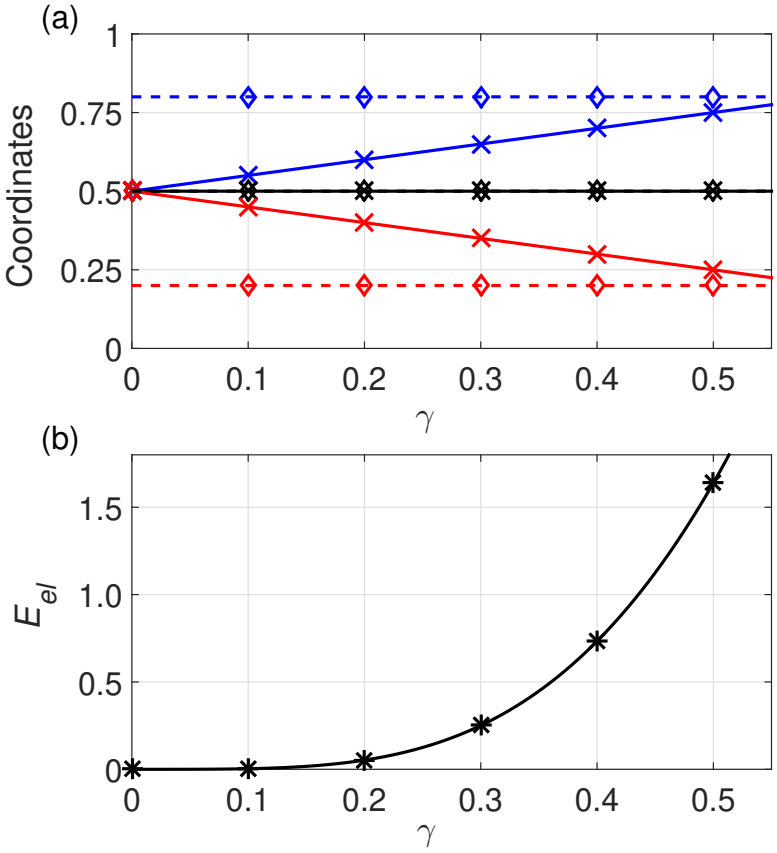

Figure 2.6: Single filament test results. (a) x and y coordinates of filament nodes B' C', and D' at elastic equilibrium state against strain γ. Solid (dashed) curves are the theoretical predictions of x (y) coordinates for B' (blue), C' (black), and D' (red), where the black solid and dashed curves overlap since C' is always at the center of the unit cell regardless of the amount of strain. The optimized x (y) coordinates of filament nodes from L-BFGS solver are shown as 'crosses' ('diamonds') of corresponding color. (b) Elastic energy against strain, where the solid curve is the theoretical prediction and 'asterisks' are the optimized elastic energies from L-BFGS solver under corresponding strain.

$(-\gamma L)$ in x direction according to the new periodic boundary conditions under shear with a parallelepiped unit cell. Due to the constraints on nodes A and E in the center unit cell, the virtual nodes of A' $(0.5L+\gamma L, 1.1L, 0.5L)$ and E' $(0.5L-\gamma L, -0.1L, 0.5L)$ are also constrained in space, however, the filament nodes B C and D are allowed to move freely until they stop at new positions of B' C' and D' where the system reaches elastic equilibrium. In the test simulation, the KMC cross-linking is turned off such that the connectivity of the nodes are maintained, only the L-BFGS solver is working to optimize the coordinates of B' C' and D'. From this model, the theoretical values of the filament node coordinates and the system elastic energy can be easily calculated from linear elasticity theory at equilibrium state, which are to compare with the corresponding values provided by L-BFGS solver. For simplicity, the unit cell size L is set as 1 *unit length*, the stretching stiffness of filament segments k_s and cross-links k are both set equal to $\frac{k_BT}{(unit\ length)^2}$, resulting in an angular spring stiffness of filament segments $\kappa_b = \frac{3\sqrt{2}}{5}k_BT$ based on Equation 2.28 and 2.30 with $\ell = 0.6L$. Obviously, the theoretical solution requires a perfect colinearity of A' B' C' D' E' and an equal separation between segments as |A'B'|=|B'C'|=|C'D'|=|D'E'|. Therefore, the coordinates of B', C' and D' at elastic equilibrium state are related to the strain γ as

$$\begin{cases} \mathrm{B}': & (\frac{1+\gamma}{2}, 0.8, 0.5) \\ \mathrm{C}': & (0.5, 0.5, 0.5) \\ \mathrm{D}': & (\frac{1-\gamma}{2}, 0.2, 0.5) \end{cases}, \tag{2.45}$$

and the elastic energy E_{el} of the system at the equilibrium configuration can also be expressed as a function of γ

$$\begin{aligned} E_{el} =& \frac{1}{2}k\left[(|\mathrm{A'B'}|-0.3)^2+(|\mathrm{D'E'}|-0.3)^2\right] \\ &+\frac{1}{2}k_s\left[(|\mathrm{B'C'}|-0.3)^2+(|\mathrm{C'D'}|-0.3)^2\right]. \\ =& 2k_BT\left(\sqrt{\frac{\gamma^2}{4}+0.09}-0.3\right)^2 \end{aligned} \tag{2.46}$$

Inspiringly, the optimal coordinates and minimized elastic energy from L-BFGS solver match the theoretical predictions particularly well, as shown in Figure 2.6. The filament-cross-link system now behaves as a nonlinear elastic material along x direction with a non-

zero shear modulus, resulting from the pure stretching of the filament and cross-links, which is essentially attributed to the constraints on nodes A and E.

The single filament system provides a simplest equivalent correspondence of a filament network, allowing us to understand the rigidity percolation transition through a visualized picture. Without constraining nodes A and E, the equilibrium elastic energy of the single filament system becomes zero regardless of the amount of strain, since now the filament-cross-link cluster behaves as a fluid particle and no deformation in ways of stretching or bending is needed to regain the elastic equilibrium. This can be treated as a naive picture of "networks" below the rigidity percolation transition, whose shear modulus is zero due to a lack of constraints from the network itself. However, simply by adding one condition that the essential connectivity between node A and E through the network exists as an effective spring, the system turns into a network above the rigidity percolation transition. As shown in Figure 2.5, right after the strain, node A (or A') is experiencing a stress along $\overrightarrow{A'B'}$ direction, while node E (or E') is stretched along $\overrightarrow{E'D'}$ direction. On the other hand, the effective spring between the essentially connected nodes A and E tends to pull them closer. The overall force on node A (E) at this elastic non-equilibrium state has a component pointing to -x (+x) direction, this relatively separating motion in x direction between the remote parts of the "network" represented by nodes A and E is exactly the shear effect. Even though the system eventually reaches a new elastic equilibrium state, the elastic energy growth due to strain cannot be fully relaxed during the elastic non-equilibrium process, since both the effective spring between nodes A and E and the filament-cross-link cluster are still stretched at the new elastic equilibrium state. Therefore, the essential connectivity between distant parts of the network (represented by nodes A and E in this single filament case) is the key to have a non-zero shear modulus.

CHAPTER 3

Stress Relaxation in 3-D Filament-constrained Network

3.1 Introduction

Semiflexible networks above the rigidity percolation transition can deform both affinely or non-affinely under shear, previous works by Levine *et al.* showed the two dimensional semiflexible networks at high cross-link density and for rigid filaments deform affinely under strain[8][9][21][22][42][23], as predicted by the classical theories of rubber elasticity, in which the strain field is uniformly distributed throughout the network. Under the affine deformation, the filaments should purely translate, rotate, stretch or compress, when assuming the cross-links are non-stretchable freely rotating rivets or rods, the strain energy of the network will be completely stored in the extensional or compressional modes of the filaments and the shear modulus of the network will be independent of the filament bending modulus. Inspired by these works on static filament networks, we are particularly interested in the stress relaxation dynamics of the networks with transient cross-links which can also store elastic energy and are able to dynamically form or break between filaments. In this chapter, we propose a model of three dimensional filament network with transient cross-links using the finite element Kinetic Monte Carlo approach we developed, and explore the dynamics of the cross-links during stress relaxation when a strain controlled shear is applied to the network through an affine deformation on the filaments. In order to maintain a static configuration of the filaments under the uniform strain field and focus on probing into the cross-linking dynamics, we constrain the filaments in space. We discuss the linear shear elasticity of the three dimensional network from both theoretical and numerical simulation perspectives.

We find the strain energy mainly arises from the deformation growth of highly-stretched cross-links orientating in certain directions, where both the number and the average elastic energy growth of these cross-links scale linearly with the strain. We also observe the strain energy dissipation through strain-guided cross-link reorganization, which results in a trained configuration of cross-links that tends to maintain the current deformation on filaments.

3.2 Network Model

We use a simple model to construct a statistically homogeneous and isotropic network of constrained filaments in three dimensions, by placing straight rods of a fixed length at random positions and orientations in a box with periodic boundary conditions applied in each direction. At an initial state, $N = 500$ filaments (each of length $\ell = 4\mu m$ and constructed by $n_f = 21$ evenly separated nodes) are randomly distributed into a $10\mu m \times 10\mu m \times 10\mu m$ unit cell. Under the assumption that the filaments are constrained is space, they now serve as a fixed breeding ground for the transient cross-links. When the system reaches equilibrium, where the average number density of cross-links and the average energy density of the network stop growing over time, we then acquire a statistically homogeneous and isotropic network of random cross-links and constrained filaments, as shown in Figure 3.1 (a). With the parameters from above, the network has a mesh size $\xi = 0.7\mu m$.

A strain controlled step shear is applied to the network at its equilibrium state through an affine deformation on the filaments, in which the filament nodes will be moved and constrained at new positions following the affine shear transformation as

$$\begin{pmatrix} r'_x \\ r'_y \\ r'_z \end{pmatrix} = \begin{bmatrix} 1 & \gamma & 0 \\ 0 & 1 & 0 \\ 0 & 0 & 1 \end{bmatrix} \begin{pmatrix} r_x \\ r_y \\ r_z \end{pmatrix}, \tag{3.1}$$

where γ is the strain, $\mathbf{r} = (r_x, r_y, r_z)^{\mathrm{T}}$ and $\mathbf{r'} = (r'_x, r'_y, r'_z)^{\mathrm{T}}$ are the position vectors of filament nodes before and after shear, respectively. In a strained state, the filaments cannot bend but are allowed to stretch or compress according to the strain field with a constant energy cost from the themselves during the entire process, however, the shear strain energy of the

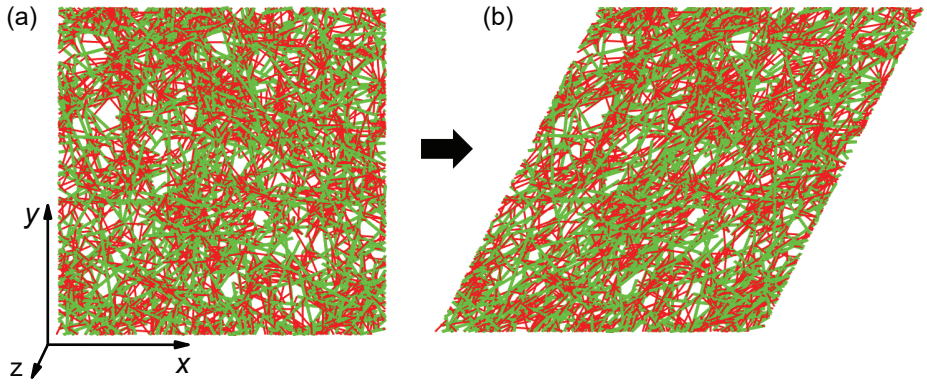

Figure 3.1: Model of the 3-D network projection view onto x-y plane showing the filaments in green and the cross-links in red. (a) Unstrained. (b) 50% step shear in $x-y$ plane along $+x$ direction is applied through the affine deformations of filaments.

network will not remain constant due to the dynamics of the cross-links. In this filament-constrained case, the elastic energy of the filaments is excluded from the expression of total elastic energy after shear, since it remains as a constant during the stress relaxation and will not be dissipated through any kind of cross-linking process. The unit cell of periodic boundary conditions is also sheared (from a cube to a parallelepiped) to cancel the offset of the filaments and cross-links that crossed the top and bottom boundaries. Figure 3.1 (b) shows the configuration of a strained network from its unstrained equilibrium state in Figure 3.1 (a).

In the simulation, the temperature is set as $T = 300K$, and the energy will be measured in k_BT unit. The cross-link spring constant k is set as $0.025pN/\mu m \approx 6k_BT/\mu m^2$, with a rest length $a_c = 0.04\mu m$ and a maximum allowed extension $a_m = 1\mu m$. The mass of a cross-link protein molecule is chosen as $1.05 \times 10^5 amu \approx 1.74 \times 10^{-22} kg$, therefore, the *thermal de Broglie wavelength* λ_B of a cross-link is $3.1 \times 10^{-7}\mu m$. The chemical binding energy ε_b between both ends of a cross-link and two filaments is set as $10kcal/mol$ and the concentration of gas phase cross-links c is set to be in the order of $10^5 \mu m^{-3}$.

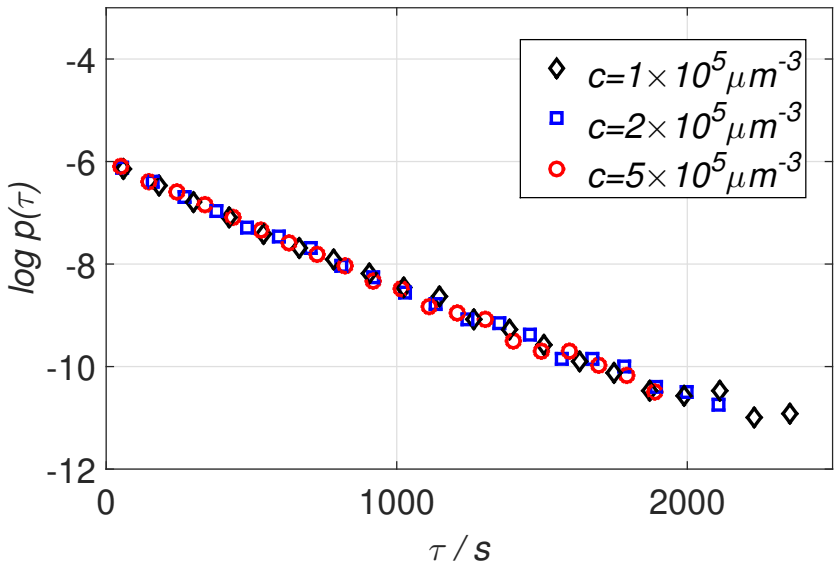

Figure 3.2: Natural logarithm plot of the empirical probability density function of bound cross-link lifetime $p(\tau)$ at different concentrations $c = 1 \times 10^5 \mu m^{-3}$ (black diamonds), $2 \times 10^5 \mu m^{-3}$ (blue squares), and $5 \times 10^5 \mu m^{-3}$ (red circles). Multiple different stochastic processes on the same configuration of filaments are averaged such that the relative error of $\delta\tau_0 = |\Delta\tau_0 / < \tau_0 > |$ is within 1%. The average bound cross-link lifetime $\tau_0 = 402.5s$ when $\nu_0 = 0.001 s^{-1}$ and $c = 1 \times 10^5 \mu m^{-3}$.

3.3 Results

3.3.1 Equilibrium state

To explore the transient nature of the cross-links during the network formation and equilibrating process, the probability density function of bound cross-link lifetime $p(\tau)$ is achieved from the empirical probability function of bound cross-link lifetime $P(\tau - \delta\tau/2, \tau + \delta\tau/2)$ with a histogram interval $\delta\tau$, following

$$P(\tau - \frac{\delta\tau}{2}, \tau + \frac{\delta\tau}{2}) = \int_{\tau - \frac{\delta\tau}{2}}^{\tau + \frac{\delta\tau}{2}} p(\tau')\, d\tau' \approx p(\tau)\delta\tau, \tag{3.2}$$

which leads to

$$p(\tau) \approx \frac{P(\tau - \frac{\delta\tau}{2}, \tau + \frac{\delta\tau}{2})}{\delta\tau}. \tag{3.3}$$

Since each cross-linking event is associated with a system time, the lifetime of a bound cross-link can be measured through taking the difference between the system time of its binding and unbinding steps. There are cross-links lived multiple lives in the network history, and each of their appearance is treated as an additional contribution to the lifetime set. Figure 3.2 shows the natural logarithm plot of $p(\tau)$ against the bound cross-link lifetime τ at different gas phase cross-link concentrations. Surprisingly, we find $p(\tau)$ follows an exponential distribution as

$$p(\tau) = \frac{1}{\tau_0} \exp(-\tau/\tau_0). \tag{3.4}$$

Even with different gas phase cross-link concentrations at this magnitude of $10^5 \mu m^{-3}$, the exponential distribution parameter τ_0 are very similar within a statistically relative error of 2%. This can be understood by the fact that the lifetime of a bound cross-link at equilibrium state is its unbinding rate ν_{off} governed when c is large and filaments are constrained. The average value of an exponential distribution $< \tau >$ is exactly τ_0, which provides a time scale for system dynamics, and choosing τ_0 as the new time unit will normalize the affects of ν_0.

With the cross-link binding and unbinding mechanism, the system starts with zero cross-link will evolve till an equilibrium state when the number density of cross-links and energy density of the network both become stable, where the relative fluctuation of the bound cross-link number $\delta N_{CL} = |\Delta N_{CL}/ < N_{CL} > |$ and the relative fluctuation of total energy $\delta E_{tot} = |\Delta E_{tot}/ < E_{tot} > |$ are, statistically, both smaller than 0.5% during $2\tau_0$ time. Since the filaments are constrained, the total energy of the network E_{tot} only contains a negative chemical binding energy of cross-links E_b when forming non-covalent bonds with filaments and a positive elastic energy E_{el} of bound cross-links. Figure 3.3 shows the evolution of number of bound cross-links N_{CL} over time and Figure 3.4 (a) shows the evolution of the total energy of the network, which decreases over time with a growing number of bound cross-links and reaches equilibrium slightly after the time when the number of bound cross-links becomes stable, the slight delay is caused by the fluctuation of elastic energy. The

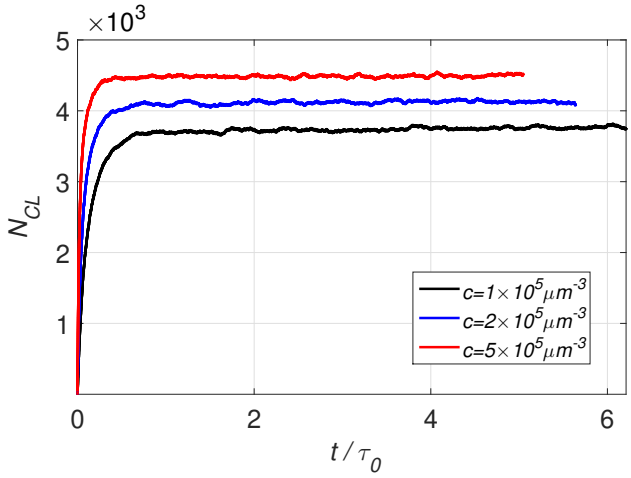

Figure 3.3: Number of bound cross-links N_{CL} in the network against time measured in τ_0 time unit at different concentrations of $c = 1 \times 10^5 \mu m^{-3}$ (black), $2 \times 10^5 \mu m^{-3}$ (blue), and $5 \times 10^5 \mu m^{-3}$ (red).

total elastic energy stored in cross-links E_{el}, as shown in Figure 3.4 (b), also grows over time until approaching an equilibrium, where the relative fluctuation $\delta E_{el} = |\Delta E_{el}/ < E_{el} > |$ is smaller than 0.7% over $2\tau_0$ time. Although the bound cross-link lifetime is concentration independent, a higher concentration will lead to an equilibrium state with a higher number of bound cross-links, a lower total energy and a higher elastic energy, as shown in Figure 3.3, Figure 3.4 (a) and (b). This is consistent with the equation of binding fraction discussed in Chapter 2, since the binding fraction $z(x) = N_B(x)/N_S(x)$ at any fixed separation x is a monotonic increasing function of c (one can check, the derivative of $z(x)$ with respect to c is always positive regardless of the value of x) and the number of possible binding sites $N_S(x)$ of any separation x is fixed under the same configuration of filaments.

The number of bound cross-links and the elastic energy of the network at equilibrium state can be estimated theoretically. Assuming the total number of the filament nodes is large, and the nodes are uniformly distributed in the box. The number of possible binding sites associated with a randomly picked node for cross-links with separation x can be measured as the number of nodes located in a spherical shell centered at the chosen node with radius

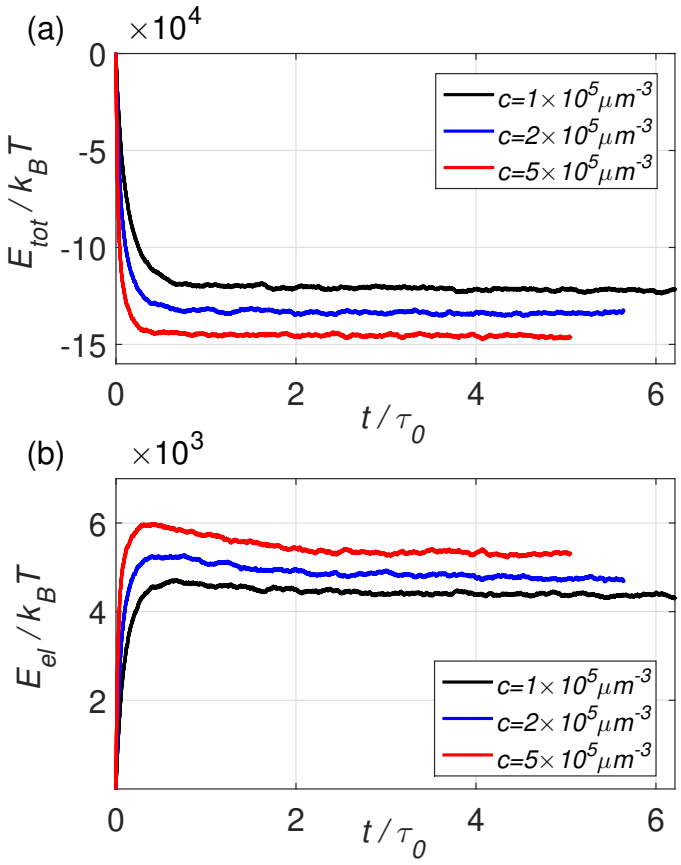

Figure 3.4: (a) Total energy E_{tot} and (b) elastic energy E_{el} in the network against time measured in τ_0 time scale at different concentrations of $c = 1\times10^5\mu m^{-3}$ (black), $2\times10^5\mu m^{-3}$ (blue), and $5 \times 10^5\mu m^{-3}$ (red).

x and thickness dx as

$$N_s(x)dx = \frac{Nn_f}{V}4\pi x^2\,dx, \tag{3.5}$$

where $\frac{Nn_f}{V}$ represents the number density of the evenly distributed filament nodes, N is the number of filaments in the system and n_f is the number of nodes on each filament. The total number of binding sites with separation x of all nodes in the system can then be expressed as

$$N_S(x)dx = \frac{Nn_f}{V}4\pi x^2\,dx\frac{Nn_f}{2}, \tag{3.6}$$

where the factor of $\frac{1}{2}$ is due to the double counting of each site. The number of bound cross-links among $N_S(x)$ possible sites following Boltzmann distribution, as discussed in Chapter

2, should be

$$N_B(x)dx = \frac{(Nn_f)^2}{2V} 4\pi x^2 \frac{c\lambda_B^3 e^{\frac{\varepsilon_b}{k_B T}} e^{-\frac{1}{2}\frac{k(x-a_c)^2}{k_B T}}}{1 + c\lambda_B^3 e^{\frac{\varepsilon_b}{k_B T}} e^{-\frac{1}{2}\frac{k(x-a_c)^2}{k_B T}}} \, dx, \tag{3.7}$$

where c is the concentration of gas phase cross-links, $\lambda_B = \frac{h}{(2\pi m k_B T)^{1/2}}$ is the *thermal de Broglie wavelength* of cross-links, ε_b is the chemical binding energy of two non-covalent bonds between both ends of the cross-link and corresponding filaments, and a_c is the equilibrium length of the cross-links.

Therefore, we can compute the total number of bound cross-links in the network by integrating $N_B(x)$ over x from a_c to the maximum allowed extension of cross-links a_m as

$$N_B = \int_{a_c}^{a_m} N_B(x)\, dx = \frac{(Nn_f)^2}{2V} \int_{a_c}^{a_m} 4\pi x^2 \frac{c\lambda_B^3 e^{\varepsilon_b} e^{-\frac{1}{2}k(x-a_c)^2}}{1 + c\lambda_B^3 e^{\varepsilon_b} e^{-\frac{1}{2}k(x-a_c)^2}} \, dx, \tag{3.8}$$

where we will measure ε_b in $k_B T$ unit and measure k in $\frac{k_B T}{length^2}$ unit to simplify the expression. The integration of averaging the orientations of the cross-links over the solid angle is 1, which is not shown in the expression, since the cross-links are considered uniformly orientated in all directions. Unfortunately, now we have included the forbidden self-links between nodes on the same filaments, by subtracting the number of self-links, we end up at a theoretical total number of bound cross-links for a system with perfectly evenly distributed nodes. With the current parameters, this number is of the same magnitude as the observed N_{CL} from simulation but greater. This fact is due to the following reason: The nodes on the same filament has to be co-linear when we produce the network, if the first two nodes on a filament are placed, it enforces an extra constraint on the rest of the $n_f - 2$ nodes to line up along the line rather than randomly choosing their coordinates. This results in observable local cavities and densely filled regions as shown in Figure 3.1 (a), indicating the absolute homogeneousness of nodes is hard to reach for filament networks.

However, we can normalize the effects of a greater number of bound cross-links due to the perfect homogeneity assumption by evaluating the probability distribution of bound cross-links with separation x as

$$p(x)dx = \frac{N_B(x)\, dx}{N_B} = \frac{x^2 \frac{c\lambda_B^3 e^{\varepsilon_b} e^{-\frac{1}{2}k(x-a_c)^2}}{1+c\lambda_B^3 e^{\varepsilon_b} e^{-\frac{1}{2}k(x-a_c)^2}} \, dx}{\int_{a_c}^{a_m} x^2 \frac{c\lambda_B^3 e^{\varepsilon_b} e^{-\frac{1}{2}k(x-a_c)^2}}{1+c\lambda_B^3 e^{\varepsilon_b} e^{-\frac{1}{2}k(x-a_c)^2}} \, dx}, \tag{3.9}$$

which can be also expressed in terms of the probability distribution of the cross-link deformation $\Delta x = x - a_c$ as

$$p(\Delta x)d(\Delta x) = \frac{(\Delta x + a_c)^2 \frac{c\lambda_B^3 e^{\varepsilon_b} e^{-\frac{1}{2}k\Delta x^2}}{1+c\lambda_B^3 e^{\varepsilon_b} e^{-\frac{1}{2}k\Delta x^2}} d(\Delta x)}{\int_0^{a_m - a_c} (\Delta x' + a_c)^2 \frac{c\lambda_B^3 e^{\varepsilon_b} e^{-\frac{1}{2}k\Delta x'^2}}{1+c\lambda_B^3 e^{\varepsilon_b} e^{-\frac{1}{2}k\Delta x'^2}} d(\Delta x')}. \tag{3.10}$$

The elastic energy of the entire network is written in terms of the summation of the elastic energies over all cross-links, which can be approximated by an integral averaging over a continuous Δx that follows the distribution of $p(\Delta x)$ as

$$\begin{aligned} E_{el} =& \sum_{i=1}^{N_{CL}} \frac{1}{2} k \Delta x_i^2 = \frac{1}{2} k N_{CL} < \Delta x_i^2 >_i \\ \approx& \frac{1}{2} k N_{CL} \int_0^{a_m - a_c} p(\Delta x) \Delta x^2 \, d(\Delta x), \end{aligned} \tag{3.11}$$

which can be calculated exactly given the parameters of cross-links and the observed number of bound cross-links at equilibrium state. Inspiringly, the elastic energies acquired from the simulation are within a 4% relative error of the theoretical predictions for all three tested gas phase cross-link concentrations. This expression also indicates the positive correlation between the network elastic energy E_{el} and the free phase cross-link concentration c, which is verified by the simulation results. From now on, only the results of $c = 1 \times 10^5 \mu m^{-3}$ will be shown since the underlying physics is c independent.

3.3.2 Linear elasticity

When a strain controlled step shear is applied to the equilibrated network through the affine deformation on filaments, the network shows a non zero shear modulus due to the overall elastic energy change of the cross-links.

Each cross-link in the network, which connects a pair of filament nodes, is also deformed affinely at the shear step. The elastic energy change of an individual cross-link can then be calculated through evaluating the change of cross-link length. Suppose a cross-link (with length x and an arbitrary orientation of polar angle θ with respect to Y axis and an azimuthal angle φ in Z-X plane) is strained affinely by γ applied in X-Y plane and along X direction,

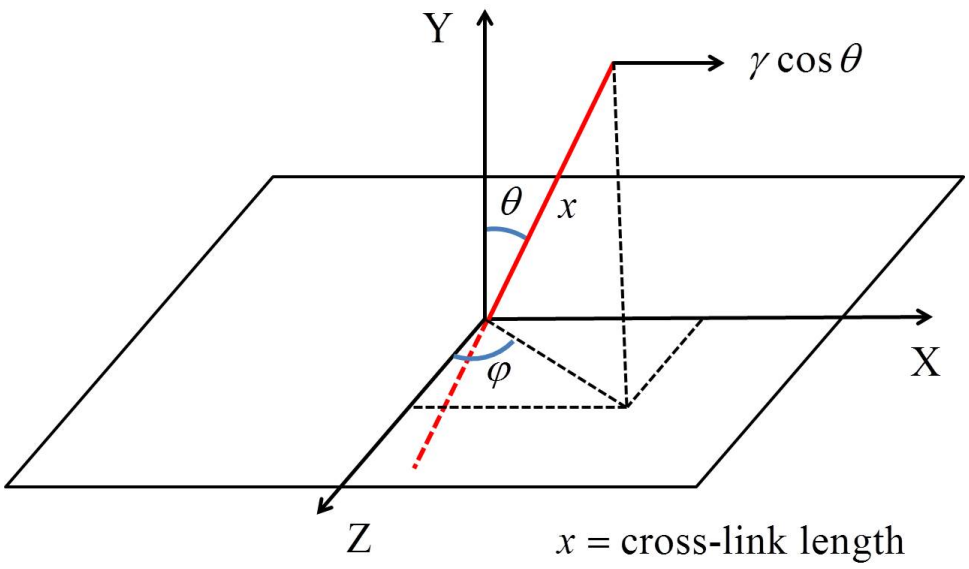

Figure 3.5: Schematic of single cross-link orientation. A cross-link with length x (red) has a polar angle θ with respect to Y axis and an azimuthal angle φ in Z-X plane. This coordinate system is chosen for the simplicity of illustrating the effects of a shear applied in X-Y plane and along X direction, which is equivalent to the normal spherical coordinate system.

as shown in Figure 3.5. This coordinate system is chosen for the simplicity of illustrating the effects of a shear applied in X-Y plane, which is equivalent to the normal spherical coordinate system. The length of the cross-link after shear x' can be expressed as

$$\begin{aligned} x' =& \sqrt{(x\sin\theta\sin\varphi + x\gamma\cos\theta)^2 + (x\cos\theta)^2 + (x\sin\theta\cos\varphi)^2} \\ =& x\sqrt{1 + 2\gamma\ \sin\theta\cos\theta\sin\varphi + \gamma^2\cos^2\theta}. \end{aligned} \tag{3.12}$$

Taylor expanding the square root leads to

$$\begin{aligned} x' \approx\ & x + x\gamma\sin\theta\cos\theta\sin\varphi + \frac{1}{2}x\gamma^2\cos^2\theta \\ & - \frac{1}{2}x\gamma^2\sin^2\theta\cos^2\theta\sin^2\varphi + xO(\gamma^3). \end{aligned} \tag{3.13}$$

The elastic energy of the affinely deformed cross-link ϵ'_{CL} at a strained state can then be

written as

$$\begin{aligned}\epsilon'_{CL} &= \frac{1}{2}k(x'-a_c)^2 \\ &\approx \frac{1}{2}k\big[(x-a_c)^2 + 2(x-a_c)x\gamma\sin\theta\cos\theta\sin\varphi \\ &\qquad + a_c x\gamma^2\sin^2\theta\cos^2\theta\sin^2\varphi \\ &\qquad + (x-a_c)x\gamma^2\cos^2\theta + O(\gamma^3)\big].\end{aligned} \tag{3.14}$$

Noticing that $x - a_c = \Delta x$ is the stretching length of the cross-link in an unstrained state, hence we can express ϵ'_{CL} in terms of Δx as

$$\begin{aligned}\epsilon'_{CL} \approx \frac{1}{2}k\Delta x^2 + \frac{1}{2}k\big[&2\Delta x(\Delta x + a_c)\gamma\sin\theta\cos\theta\sin\varphi \\ &+ a_c(\Delta x + a_c)\gamma^2\sin^2\theta\cos^2\theta\sin^2\varphi \\ &+ \Delta x(\Delta x + a_c)\gamma^2\cos^2\theta + O(\gamma^3)\big],\end{aligned} \tag{3.15}$$

where the first term $\frac{1}{2}k\Delta x^2 = \epsilon_{CL}$ is the elastic energy stored in the cross-link in an unstrained state. Therefore, the elastic energy change of this cross-link $\Delta\epsilon_{CL} = \epsilon'_{CL} - \epsilon_{CL}$ is a function of γ, Δx, θ, and φ as (if ignoring the third or higher order corrections of γ)

$$\begin{aligned}\Delta\epsilon_{CL}(\gamma,\Delta x,\theta,\varphi) \approx\ & k\gamma\Delta x(\Delta x + a_c)\sin\theta\cos\theta\sin\varphi \\ &+\frac{1}{2}k\gamma^2\big[a_c(\Delta x + a_c)\sin^2\theta\cos^2\theta\sin^2\varphi \\ &\qquad + \Delta x(\Delta x + a_c)\cos^2\theta\big].\end{aligned} \tag{3.16}$$

The strain energy of the entire network U consisting of the elastic energy change from all cross-links (where the stretching or compressing energy of the filaments are excluded as discussed in Section 3.2) can be written as

$$\begin{aligned}U =& \sum_{i=1}^{N_{CL}} \Delta\epsilon_{CL,i} = N_{CL} < \Delta\epsilon_{CL,i} >_i \\ \approx& N_{CL} < \Delta\epsilon_{CL}(\gamma,\Delta x,\theta,\varphi) >_{\Delta x,\theta,\varphi} \\ =& N_{CL}\int_0^{a_m - a_c} d(\Delta x)\int_{-1}^{1} d(-\cos\theta)\int_0^{2\pi} d\varphi\ \frac{p(\Delta x)}{4\pi}\Delta\epsilon_{CL}(\gamma,\Delta x,\theta,\varphi),\end{aligned} \tag{3.17}$$

where $< \Delta\epsilon_{CL,i} >_i$ is approximated by the integral averaging over a continuous Δx following the distribution of $p(\Delta x)$ given by Equation 3.10 and over a uniformly distributed cross-link orientations in three dimensions. Cross-links with any stretching lengths are assumed having

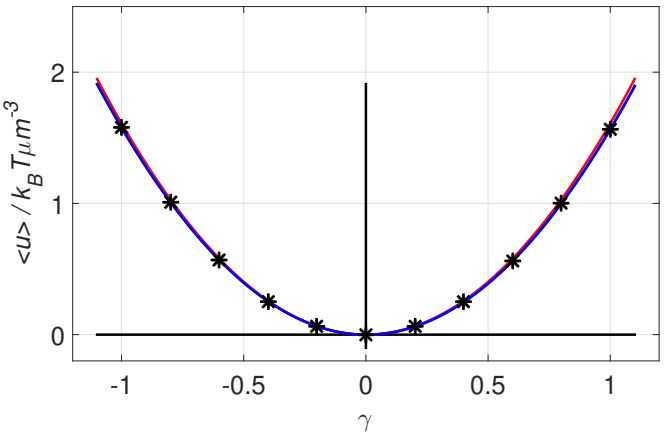

Figure 3.6: Average strain energy density $< u >$ against strain γ (applied in $X - Y$ plain along X direction), with data points at γ =-1, -0.8, -0.6, -0.4, -0.2, 0, 0.2, 0.4, 0.6, 0.8, 1.0 (black asterisks) and a fitting curve (blue solid) of function $< u >= \frac{1}{2}G(\gamma - \gamma_0)^2 + u_0$, which gives $\gamma_0 \approx 0$, $u_0 \approx 0$ and the shear modulus $G = 3.14 k_B T \mu m^{-3}$ with an average fitting error of $4 \times 10^{-4} k_B T \mu m^{-3}$ per data point. The theoretical prediction curve (red solid) is based on the shear modulus given by Equation 3.20, which is $3.22 k_B T \mu m^{-3}$. The gas phase cross-link concentration c is set to be $1 \times 10^5 \mu m^{-3}$.

an equal probability orienting to any directions of the 4π solid angle, which results in the factor of $\frac{1}{4\pi}$ in the expression of the three-dimensional probability distribution.

By plugging Equation 3.16 into Equation 3.17, the linear term of γ vanishes, which is also implied by the symmetry of the problem, leading to a quadratic dependence of U and γ as

$$\begin{aligned} U &\approx \frac{1}{2}\gamma^2 k N_{CL}\Bigg[\int_0^{a_m - a_c} a_c(\Delta x + a_c)p(\Delta x)\, d(\Delta x) \int_0^{\pi} \frac{\sin^3\theta \cos^2\theta}{2}\, d\theta \int_0^{2\pi} \frac{\sin^2\varphi}{2\pi}\, d\varphi \\ &\qquad + \int_0^{a_m - a_c} \Delta x(\Delta x + a_c)p(\Delta x)\, d(\Delta x) \int_0^{\pi} \frac{\sin\theta \cos^2\theta}{2}\, d\theta \int_0^{2\pi} \frac{1}{2\pi}\, d\varphi\Bigg] \\ &= \frac{1}{2}\gamma^2 k N_{CL}\Bigg[\frac{1}{15}\int_0^{a_m - a_c} a_c(\Delta x + a_c)p(\Delta x)\, d(\Delta x) \\ &\qquad + \frac{1}{3}\int_0^{a_m - a_c} \Delta x(\Delta x + a_c)p(\Delta x)\, d(\Delta x)\Bigg]. \end{aligned} \tag{3.18}$$

The average strain energy density $< u >= U/V$ takes the form as

$$< u >= \frac{1}{2} G\gamma^2, \tag{3.19}$$

with a constant shear modulus of

$$\begin{aligned} G = \frac{kN_{CL}}{V}\Bigg[\frac{1}{15}\int_0^{a_m-a_c} a_c(\Delta x + a_c)p(\Delta x)\, d(\Delta x) \\ + \frac{1}{3}\int_0^{a_m-a_c} \Delta x(\Delta x + a_c)p(\Delta x)\, d(\Delta x)\Bigg], \end{aligned} \tag{3.20}$$

where k is the cross-link spring stiffness, N_{CL} is the number of bound cross-link in the network, V is the volume of the system, $p(\Delta x)$ is the probability density function of cross-links with stretching length Δx at an unstrained equilibrium state, a_c is the rest length of the cross-links, and a_m is the maximum allowed length of the cross-links.

From the simulation results, the network indeed behaves as a linear shear elastic material, and an identical constant shear modulus in all directions for networks with the same filament and cross-link configurations is observed within a statistical relative error of 2%. Multiple different stochastic cross-linking processes upon the same filaments configuration are also averaged, such that the statistical relative error of shear modulus $\delta G = |\Delta G/ < G > |$ of different cross-link configurations at equilibrium state is within 2%. The shear modulus generated from simulations is also within a 2.5% relative error of the theoretical prediction given by Equation 3.20. Therefore, from a shear elasticity perspective, the cross-linked network model is proved statistically homogeneous and isotropic, as expected. Figure 3.6 shows the average strain energy density $< u >$ scales quadratically with the strain γ and the proportionality constant is equal to $G/2$.

Applying different amount of strain on the same network results in distinct bound cross-link elastic energy distributions, especially, with significantly unique tails of high elastic energy cross-links. The empirical probability function of the elastic energy of bound cross-links can be written as

$$P(\epsilon_{CL} - \frac{\delta\epsilon_{CL}}{2}, \epsilon_{CL} + \frac{\delta\epsilon_{CL}}{2}) = \int_{\epsilon_{CL}-\frac{\delta\epsilon_{CL}}{2}}^{\epsilon_{CL}+\frac{\delta\epsilon_{CL}}{2}} p(\epsilon'_{CL})\, d\epsilon'_{CL} \approx p(\epsilon_{CL})\delta\epsilon_{CL}, \tag{3.21}$$

where $\delta\epsilon_{CL}$ is the histogram interval and $p(\epsilon_{CL})$ is the empirical probability density function of cross-link elastic energy, from which we can approximate the $p(\epsilon_{CL})$ from the simulation

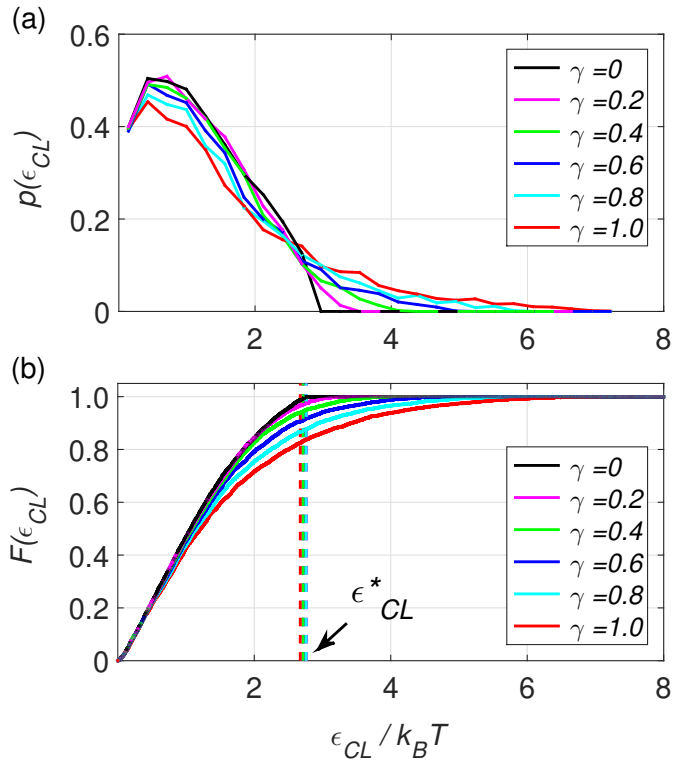

Figure 3.7: (a) Empirical probability density functions of bound cross-link elastic energy $p(\epsilon_{CL})$ at strain $\gamma = 0$ (black), 0.2 (magenta), 0.4 (green), 0.6 (blue), 0.8 (cyan), and 1.0 (red), with a histogram interval $\delta\epsilon_{CL} = 0.28k_BT$. (b) Empirical (cumulative) distribution functions of bound cross-link elastic energy $F(\epsilon_{CL})$ shown as solid curves at strain $\gamma = 0$ (black), 0.2 (magenta), 0.4 (green), 0.6 (blue), 0.8 (cyan), and 1.0 (red), the critical cross-link elastic energies ϵ^*_{CL} indicating the starting point of distribution tails are labeled by dashed lines of the corresponding color. The five dashed lines look overlapping since the relative error of $\delta\epsilon^*_{CL} = |\Delta\epsilon^*_{CL}/ < \epsilon^*_{CL} > |$ is smaller than 1.5%, and they all locate within a 3.0% relative error around the maximum cross-link elastic energy at an unstrained equilibrium state following $\epsilon^*_{CL} \approx \sup(\epsilon_{CL,\gamma=0})$.

data as

$$p(\epsilon_{CL}) \approx \frac{P(\epsilon_{CL} - \frac{\delta\epsilon_{CL}}{2}, \epsilon_{CL} + \frac{\delta\epsilon_{CL}}{2})}{\delta\epsilon_{CL}}. \tag{3.22}$$

A greater strain results in a wider distribution of cross-links elastic energy with less low-energy cross-links and more high-energy cross-links, as shown in Figure 3.7 (a). In order to determine whether the two samples of the elastic energy of cross-links before and after strain are statistically different, we employ a 'two-sample Kolmogorov-Smirnov test' (K-S test) to acquire a simple standard[73][74], which is the critical significance level of incorrectly differing these two cross-link elastic energy distributions.

The basic idea of 'two-sample K-S test' is comparing the largest difference between the two empirical distribution functions with a critical value, which is related to a prescribed significance level and the sample sizes. The empirical distribution function of bound cross-link elastic energy $F_n(\epsilon_{CL})$ for a given network state with n cross-links is defined as

$$F_n(\epsilon_{CL}) = \frac{1}{n}\sum_{i=1}^{n} I_{[-\infty,\epsilon_{CL}]}(\epsilon'_{CL,i}), \tag{3.23}$$

where $I_{[-\infty,\epsilon_{CL}]}(\epsilon'_{CL,i})$ is the indicator function, equal to 1 if $\epsilon'_{CL,i} < \epsilon_{CL}$ and equal to 0 otherwise. And the Kolmogorov-Smirnov test statistic is chosen as

$$D_{n,m} = \sup_{\epsilon_{CL}} |F_{1,n}(\epsilon_{CL}) - F_{2,m}(\epsilon_{CL})|, \tag{3.24}$$

where $F_{1,n}$ and $F_{2,m}$ are the empirical distribution functions of the cross-link elastic energy at state I (n cross-links) and state II (m cross-links), in the case of step shear, $n = m$ since no cross-linking event occurs during an instant step strain, and **sup** is the supremum function. With a prescribed significance level α of incorrectly differing these two distributions, the two distributions are considered different with a probability $1 - \alpha$ if

$$D_{n,m} > C(\alpha)\sqrt{\frac{n+m}{nm}}, \tag{3.25}$$

where $C(\alpha) = \sqrt{-\frac{1}{2}\ln\alpha}$.

On the other hand, from $D_{n,m}$ of the given cross-link elastic energy distributions before and after shear, it is straightforward to find a critical significance level α^* such that

$$D_{n,m} = C(\alpha^*)\sqrt{\frac{n+m}{nm}}. \tag{3.26}$$

The physical meaning of α^* is the minimum significance level we can choose that the two distributions are still considered statistically different, which can be used to measure the statistical distinction between the two distributions providing identical sample sizes respectively, where $1-\alpha^*$ is the trust level (a probability) that they are statistically distinct. At the strain step, the sample sizes (number of cross-links) associated with different amount of strain are the same, therefore, α^* of each strain should indicate the essential distinction of the cross-link elastic energy distributions before and after shear.

From the simulation, $\alpha^* = 9.1\times10^{-2}$, 7.1×10^{-5}, 2.0×10^{-12}, 8.8×10^{-26}, and 1.8×10^{-44} for $\gamma = 0.2,\ 0.4,\ 0.6,\ 0.8$, and 1.0 respectively. α^* approaches to zero non-linearly and quickly when γ gets larger for the same cross-link configuration, therefore, a grater strain results in a more distinct distribution of bound cross-link elastic energy. Additionally, for networks with the same mesh size, the same bound cross-link number density, and the same elastic energy density, a decreasing $\alpha^* = \exp(-nD_{n,n}^2)$ is observed with an increasing network size V, since $D_{n,n}$ approaches to a non-zero constant with an increasing V while the number of bound cross-links n scales linearly with V. From this observation, even for small strain, the distributions are still considered different with a large enough network size, however, as expected, a larger network size means more computational-consuming. Overall, the bound cross-link elastic energy distributions before and right after a step shear are essentially different and they become more distinct when strain increases.

The empirical distribution functions of elastic energy of bound cross-links before and right after a step strain also provide a criterion to label the distribution tail of high elastic energy cross-links. The starting point of the distribution tail at an arbitrary strain is defined as the critical cross-link elastic energy ϵ_{CL}^* which leads to the largest difference between the two empirical distribution functions before and after shear, such that

$$|F_{1,n}(\epsilon_{CL}^*) - F_{2,m}(\epsilon_{CL}^*)| = D_{n,m} = \sup_{\epsilon_{CL}} |F_{1,n}(\epsilon_{CL}) - F_{2,m}(\epsilon_{CL})|. \tag{3.27}$$

By this definition, interestingly, the critical cross-link elastic energies ϵ_{CL}^* of different strains end up identical with a relative error $\delta\epsilon_{CL}^* = |\Delta\epsilon_{CL}^*/ < \epsilon_{CL}^* > |$ smaller than 1.5%, and they all locate around the maximum cross-link elastic energy at an unstrained equilibrium state

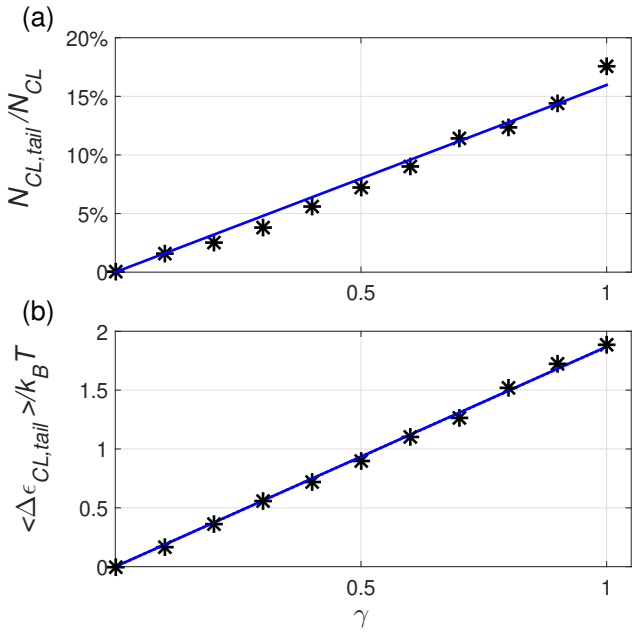

Figure 3.8: (a) The tail fraction $N_{CL,tail}/N_{CL}$ plot against strain γ, with data points (black asterisks) at $\gamma = 0,\ 0.1,\ 0.2,\ 0.3,\ 0.4,\ 0.5,\ 0.6,\ 0.7,\ 0.8,\ 0.9$, and 1.0, and a linear fitting function (blue solid) of $N_{CL,tail}/N_{CL} = b_1\gamma$ with $b_1 = 16.0\%$ and an average fitting error of 0.5% per data point. (b) The average elastic energy growth of tail cross-links $< \Delta\epsilon_{CL.tail} >$ against γ at $\gamma = 0,\ 0.1,\ 0.2,\ 0.3,\ 0.4,\ 0.5,\ 0.6,\ 0.7,\ 0.8,\ 0.9$, and 1.0, with data points (black asterisks) and a linear fitting function (blue solid) of $< \Delta\epsilon_{CL.tail} >= b_2\gamma$ with $b_2 = 1.87k_BT$ and an average fitting error of $0.02k_BT$ per data point.

within a 3.0% relative error following

$$\epsilon^*_{CL} \approx \sup(\epsilon_{CL,\gamma=0}). \tag{3.28}$$

The empirical distribution functions of cross-link elastic energy under different strain $F(\epsilon_{CL})$ are shown as the solid curves in Figure 3.7 (b), and the critical cross-link elastic energies ϵ^*_{CL} are labeled by the dashed lines.

High-energy tail cross-links play a significant role in contributing the strain energy of the network, and the average elastic energy growth of the tail cross-links scales with strain in a completely different way as the the non-tail low-energy cross-links. From the simulation, a tail cross-link fraction $N_{CL,tail}/N_{CL}$ of 2.5% (5.6%, 9.0%, 12.4%, and 17.6%) contributes

56.5% (62.0%, 66.8%, 71.3%, and 79.9%) of the total strain energy at strain $\gamma = 0.2$ (0.4, 0.6, 0.8, and 1.0), where the ratio of the average elastic energy growth per cross-link of non-tail and tail cross-links $< \Delta\epsilon_{CL,non-tail} > / < \Delta\epsilon_{CL,tail} >$ is only 2.0% (3.7%, 4.9%, 5.7%, and 5.4%). This phenomenon of the distribution tail dominating the shear strain energy can be understood in terms of the following: A small fraction of cross-links (tail cross-links) obtaining large growth in stretching length due to the affine deformation are the main contributors to the network strain energy, while a large portion of cross-links (non-tail cross-links) acquiring small or negative change in stretching length overall contribute little strain energy. If assuming the rest length of cross-links is small ($a_c \to 0$), from Equation 3.16, the elastic energy change of a cross-link can be approximated as

$$\Delta\epsilon_{CL}(\gamma, \Delta x, \theta, \varphi) \approx k\gamma\Delta x^2 \sin\theta\cos\theta\sin\varphi + \frac{1}{2}k\gamma^2\Delta x^2\cos^2\theta. \tag{3.29}$$

The tail cross-links gaining large and positive $\Delta\epsilon_{CL}$ are the ones with long stretching lengths Δx and orientating at a solid angle around $(\theta = \frac{1}{2}\arctan\frac{2}{\gamma}, \varphi = \frac{\pi}{2})$ at the unstrained state, while a same number of cross-links in the non-tail region orientating around a solid angle of $(\theta = \frac{1}{2}\arctan\frac{2}{\gamma} + \frac{\pi}{2}, \varphi \approx \frac{\pi}{2})$ shrink most and make negative contributions to the strain energy. The orientation angles that leads to the extrema of $\Delta\epsilon_{CL}$ can be determined by evaluating the first and second order derivatives of Equation 3.29. The rest of the cross-links in the non-tail region which acquire little deformation changes (positive or negative) mainly translate or rotate under the affine strain field. However, the overall elastic energy change of the non-tail cross-links is still positive due to the symmetry breaking quadratic term in Equation 3.29, and the non-tail cross-links together contribute a small portion to the strain energy of the network.

The size of distribution tails, measured by the tail cross-link fraction $N_{CL,tail}/N_{CL}$, grows linearly with γ in the regime of $\gamma \leq 1$, as shown in Figure 3.8 (a). However, the linear relation cannot be valid at large strain regime, since $N_{CL,tail}/N_{CL}$ should converge to 1 when $\gamma \to \infty$. We can also obtain an average elastic energy growth of tail cross-links $< \Delta\epsilon_{CL.tail} >$ by averaging over the differences of their elastic energies between a strained state and the unstrained state, and $< \Delta\epsilon_{CL.tail} >$ can be used to measure the average contribution per

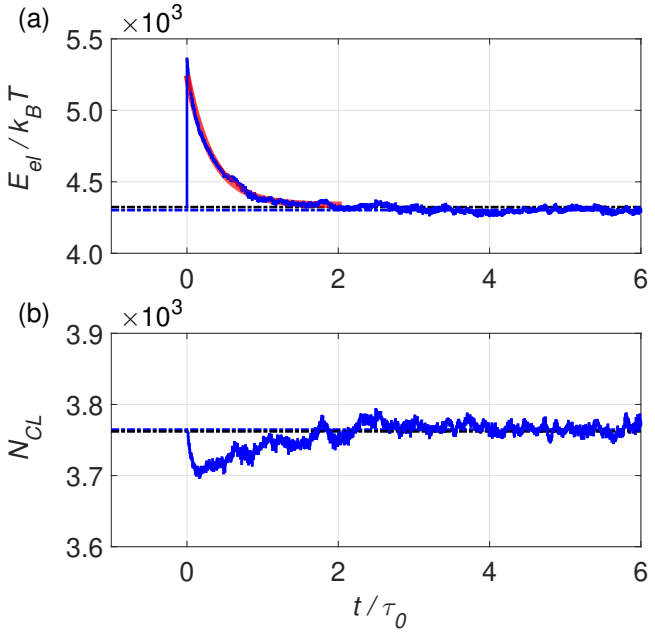

Figure 3.9: (a) Elastic energy E_{el} relaxation (blue solid curve) measured in τ_0 time unit when a step strain of 0.8 is applied at $t = 0$, multiple stochastic cross-linking processes of the same strained network are averaged such that the average relative errors $< \delta E_{el,\delta t} >_{6\tau_0} = < |\Delta E_{el,\delta t}/ < E_{el} >_{\delta t} | >_{6\tau_0}$ of each time interval $\delta t = \tau_0/500$ is within 1%. The equilibrium elastic energy before (after) shear is shown as the black dash-dot line (blue dash-dot line) with a relative fluctuation of 0.7% (0.7%), achieved through averaging E_{el} at the unstrained (strained) equilibrium state from $t = -2\tau_0$ to $t = 0$ ($t = 4\tau_0$ to $t = 6\tau_0$). An exponential decay fitting curve (red) on data points from $t = 0$ to $t = 2\tau_0$ of function $E_{el} = E^0_{el} + U \exp(-t/\tau_{rlx})$ is also plotted with an average of relative fitting error per data point smaller than 0.3% and a strain energy relaxation time constant $\tau_{rlx} \approx 0.3\tau_0$. (b) Number of bound cross-links (blue solid curve) against time, the same statistical averaging method is used as for part (a). The relative difference between the number of cross-links at the equilibrium states before (black dash-dot line) and after (blue dash-dot line) shear is within their relative fluctuations of 0.18%, so the two dash-dot lines look overlapping.

cross-link in the tail to the total strain energy. Surprisingly, $< \Delta\epsilon_{CL.tail} >$ also scales linearly with γ in the same regime of $\gamma \leq 1$, as shown in Figure 3.8 (b). Although the average elastic energy growth of all cross-links $< \Delta\epsilon_{CL} >$ scales quadratically with γ from Equation 3.18 and Figure 3.6, the tail cross-links contribute to the total strain energy quadratically with γ in a dramatically different way of scaling linearly with γ both in quantities and magnitudes of the elastic energy growth.

3.3.3 Strain energy relaxation

The fundamental microscopic cross-link binding and unbinding mechanism provides the foundation of macroscopic strain energy relaxation, where the cross-links storing large elastic energy from the step strain carry a higher probability to detach and leave the corresponding nodes free to serve as new possible binding sites for low elastic energy cross-links. This local cross-link reorganization statistically results in a strain energy relaxation toward the equilibrium at a network scale.

As shown in Figure 3.9 (a), a step strain of 0.8 is applied to the network at $t = 0$, the overall elastic energy of the network decays exponentially as

$$E_{el} = E_{el}^{0} + U \exp(-t/\tau_{rlx}), \tag{3.30}$$

until it reaches the same value as an unstrained equilibrium state, where E_{el}^{0} is the elastic energy at equilibrium state, U is the strain energy, and τ_{rlx} is the exponential relaxation time constant. The relative difference between the equilibrium elastic energies before and after shear is within their relative fluctuations of 0.7%, therefore, the equilibrium elastic energies of the unstrained and strained networks are considered statistically identical.

At the very beginning of the relaxation, both the binding and unbinding rates had a step jump comparing with their values at the unstrained equilibrium state, but the unbinding rate jumps higher than the binding rate. During the relaxation, both binding and unbinding rates decay to the same value as the unstrained equilibrium state during the same amount of time, however, the unbinding rate decays faster than the binding rate and their difference changes sign at a time shorter than τ_{rlx}. This results in a first decreasing and then increasing

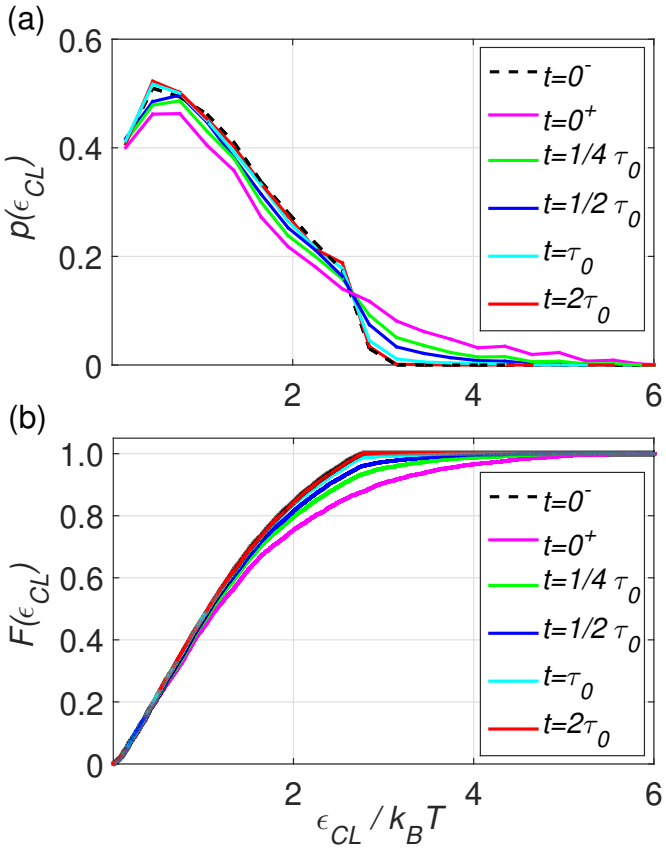

Figure 3.10: (a) Empirical probability density functions of bound cross-link elastic energy $p(\epsilon_{CL})$ at $t = 0^-$ (just before shear, black dash), $t = 0^+$ (just after shear, magenta), $t = \tau_0/4$ (green), $t = \tau_0/2$ (blue), $t = \tau_0$ (cyan), and $t = 2\tau_0$ (red), with a histogram interval $\delta\epsilon_{CL} = 0.3k_BT$. (b) Empirical (cumulative) distribution functions of bound cross-link elastic energy $F(\epsilon_{CL})$ at $t = 0^-$ (black dash), $t = 0^+$ (magenta), $t = \tau_0/4$ (green), $t = \tau_0/2$ (blue), $t = \tau_0$ (cyan), and $t = 2\tau_0$ (red), where the black and red curves look overlapping since the critical significance level α^* between these two distributions is 0.53.

number of bound cross-links during the strain energy relaxation, and the number of bound cross-links eventually reaches the same value as the unstrained equilibrium state, as shown in Figure 3.9 (b). The undulation of number of bound cross-links can be understood in terms of the 'unlocking mechanism': The strain-driven unbinding events of high elastic energy cross-links govern the cross-linking dynamics right after shear and leave corresponding spots unlocked and available for low energy cross-links to bind afterwards. A recovery of the number of bound cross-links starts when enough possible binding spots are released over time and the tendency to recover equilibrium surpasses the tendency of strain-driven unbinding, where the strained equilibrium state should carry the same cross-link number density as the unstrained equilibrium state since the density of the nodes is preserved under strain.

This strain-driven cross-link reorganization can be revealed from the empirical probability density functions of the cross-link elastic energy at time steps in a chronological order during the relaxation, as shown in Figure 3.10 (a). The unbinding events of high elastic energy cross-links in the distribution tail release their strain energy during the relaxation, which are responsible for the strain energy decay. On the other hand, the binding events of low elastic energy cross-links between the unlocked spots in the non-tail region recover the equilibrium state, which slow down the strain energy decay.

The empirical cumulative distribution functions of the cross-link elastic energy of the unstrained state ($t = 0^-$), the time just after shear ($t = 0^+$), at $t = \tau_0/4$, $t = \tau_0/2$, $t = \tau_0$, and $t = 2\tau_0$ are shown in Figure 3.10 (b). The critical significance level $\alpha^* = 8.8 \times 10^{-26}$ (5.6×10^{-13}, 1.4×10^{-5}, 0.21, and 0.53) if a two-sample K-S test is performed between the distributions at $t = 0^-$ and $t = 0^+$ ($t = \tau_0/4$, $t = \tau_0/2$, $t = \tau_0$, and $t = 2\tau_0$). The distinctions of the distributions comparing with the unstrained equilibrium state decrease over time during the relaxation, if a trust level of 99.9% ($\alpha = 0.001$) is chosen, the distributions at $t = 0^-$ and $t = 0^+$ (or $t = \tau_0/4$, $t = \tau_0/2$) are statistically different, while the distributions at $t = 0^-$ and $t = \tau_0$ (or $t = 2\tau_0$) are statistically identical. Therefore, an affine deformation field on the filaments results in a distinct bound cross-link elastic energy distribution, while the strain energy relaxation eventually recovers the distribution of the unstrained equilibrium state.

Besides the energy relaxation of the cross-links, the cross-links also recover their isotropy and orientational symmetry during the relaxation, which were broken at the stain step.

The broken symmetries can be illustrated from a 2-D model: Suppose cross-links with an arbitrary length x are uniformly orientated in the plane at the unstrained equilibrium state, we assume the midpoints of the cross-links are at $(0,0)$ in a cross-link space, the end nodes of the cross-links will be evenly distributed on a circle with a radius $\frac{x}{2}$ centered at $(0,0)$ point, the X and Y components of the cross-link end nodes r_X and r_Y should follow equation

$$r_X^2 + r_Y^2 = \left(\frac{x}{2}\right)^2. \tag{3.31}$$

If an affine deformation γ is applied along X direction to all the cross-links, the new X and Y components of the corresponding cross-link nodes become $r'_X = r_X + \gamma r_Y$ and $r'_Y = r_Y$, the nodes will be translate onto a tilted ellipse following equation

$$(r'_X - \gamma r'_Y)^2 + {r'_Y}^2 = \left(\frac{x}{2}\right)^2. \tag{3.32}$$

The isotropy of cross-links is broken under the affine strain field, since the cross-links along the major axis of the tilted ellipse has a longer length than the ones along the minor axis. To demonstrate the orientational symmetry breaking due to strain, we will switch to the polar coordinate system and set $\frac{x}{2} = r$ for simplicity, the end nodes of cross-links can be written as $(r\cos\theta, r\sin\theta)$, the nodes under stain field γ will be translated to

$$\begin{cases} r'\cos\theta' = & r\cos\theta + \gamma r\sin\theta \\ r'\sin\theta' = & r\sin\theta \end{cases}, \tag{3.33}$$

solving for the new polar coordinates r' and θ' gives

$$\begin{cases} r' = & r\sqrt{1+\gamma^2\sin^2\theta + 2\gamma\sin\theta\cos\theta} \\ \theta' = & \arcsin\left(\frac{\sin\theta}{\sqrt{1+\gamma^2\sin^2\theta+2\gamma\sin\theta\cos\theta}}\right) \end{cases}. \tag{3.34}$$

The polar angle θ at the unstrained state is uniformly distributed as $p(\theta)\,d\theta = \frac{1}{2\pi}\,d\theta$, so the distribution of the new polar angle θ' at the strained state is $p(\theta')\,d(\theta') = p(\theta_{(\theta')})\frac{d\theta}{d\theta'}\,d\theta' = \frac{1}{2\pi}\frac{d\theta}{d\theta'}\,d\theta'$, which is no longer uniform due to the implicit dependence of θ as a function θ'

suggested by Equation 3.34. Therefore, the orientational symmetry of the cross-links is also broken at the step strain. In 3-D, these arguments still hold and the equivalent analogues of the circle and the ellipse will be a sphere and an ellipsoid.

From the simulation, we find the relaxation of these strained cross-links (with length x at the unstrained equilibrium state) tends to recover the sphere (with radius $\frac{x}{2}$) from the tilted ellipsoid. If holding the step strain long enough (at least $10\tau_{rlx}$), the cross-links in the network will be eventually trained in a manner that the current strained state becomes the new lowest strain energy state of the network. Since the filament nodes are kept homogeneous under strain, Equation 3.10 is still valid at the strained equilibrium state, indicating the cross-links eventually become isotropic again at the new equilibrium state, where the orientational symmetry is also restored. This is also consistent with the fact that the number of cross-links and the total elastic energy at the strained equilibrium state both equal to the values of the unstrained equilibrium state. We also find the network after training still behaves as a linear shear elastic material with the same shear modulus, and in the direction of training we observe

$$< u' >= \frac{1}{2} G \gamma'^2, \tag{3.35}$$

where $< u' >$ is the average strain energy density if an extra strain γ' is applied on top of a network under training strain γ_0, and G is the shear modulus statistically identical to the unstrained equilibrium state. Both $< u' >$ and G are the training strain γ_0 independent.

Overall, during the relaxation, the strain energy dissipates through the strain-driven unbinding events of high elastic energy cross-links, the elastic equilibrium is recovered through the binding events of low elastic energy cross-links, and the isotropy of the cross-links is also restored.

3.4 Discussion

In this chapter, we apply the kinetic Monte Carlo method to explore the stress relaxation of filament-constrained networks with transient cross-links. We find the unstrained network at equilibrium state exhibits linear shear elasticity under affine strain field, and we explain the

fact from a theoretical approach. During the stress relaxation, the strain energy dissipates exponentially through the strain-driven unbinding of the cross-links, and the cross-links reorganize themselves to recover the equilibrium state, which contains the same number of cross-links and has the same distribution of cross-link elastic energy as the unstrained equilibrium state. The isotropy and orientational symmetry of the cross-links are broken at the step strain, while the stress relaxation macroscopically restores an isotropic configuration of cross-links and trains the network in a manner such that it prefers staying at the current strained state. We find he trained network still behaves as a linear shear elastic material with a same shear modulus as the unstrained equilibrium state, and the modulus is the training strain independent.

CHAPTER 4

Formation of Bundles in Semiflexible Network

4.1 Introduction

Cytoskeleton networks of semiflexible biopolymers are commonly seen in eukaryotic cells, and they play a crucial role in cell mechanics. These semiflexible networks typically form bundles in the presence of cross-linking molecules, which is widely observed in experiments[75][76][77][78] and studied by Brownian dynamics simulation approaches[35][60][61]. In this chapter, we propose a three-dimensional model of semiflexible filament network with transient cross-links, and explore the dynamics of the bundle formation employing the finite element kinetic Monte Carlo simulation method we developed. Comparing with a control group of filament-constrained network, we find the cross-linking dynamics is highly enhanced and the number of bound cross-links increases dramatically during the bundling process. We also find, in the time-domain where the bundles grow rapidly, the growth rates of the average (length) density of the bundles and the average energy density of the bundles are both constant, leading to a linear relation between the average density and the average energy density of the bundles. This observation indicates per unit length growth of bundled filaments contributes a constant elastic energy to the bundle regardless of the current density of the bundles, and the contribution factor is also time-independent.

4.2 Network Model

We use a similar method as for Chapter 3 to construct a statistically homogeneous and isotropic initial state of semiflexible network in three dimensions, by placing straight filaments

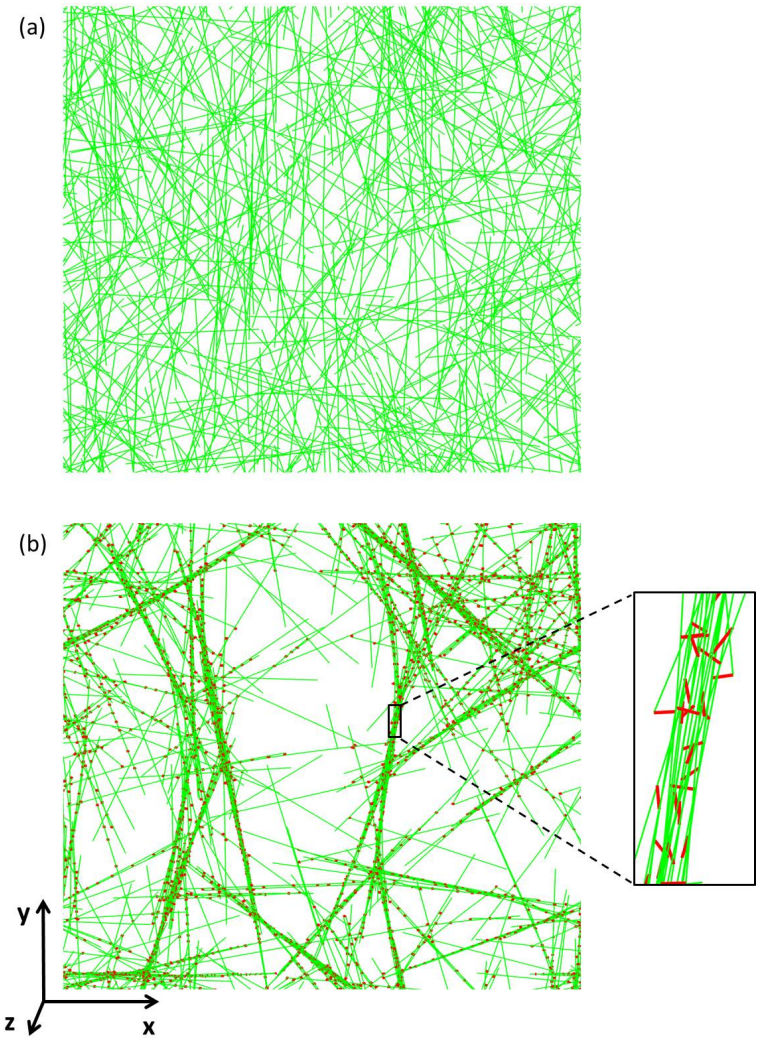

Figure 4.1: (a) Initial configuration of filaments at $t = 0s$ (projected view on x-y plane). (b) Network configuration at $t = 1000s$ showing the filaments in green and the cross-links in red.

of a fixed length at random positions and orientations in a box with periodic boundary conditions applied in each direction. At an initial state, $N = 500$ filaments (each of length $\ell = 4\mu m$ and constructed by $n_f = 21$ evenly separated nodes) are randomly distributed into a $10\mu m \times 10\mu m \times 10\mu m$ unit cell. However, differing from Chapter 3, the filaments are free to translate, rotate, stretch/compress, and bend due to the the local unbalanced forces resulting from cross-linking. In order to explore the affects of cross-linking on the network structure and elastic energy, we also set up a control group for the network, where the initial configuration of filaments are exactly the same but the filaments are constrained in space. With the parameters from above, both networks have a mesh size $\xi = 0.7\mu m$.

In the simulation, the persistence length of the filament ℓ_p is set to be $10\mu m$, and the angular spring stiffness κ_b and linear springs stiffness k_s of filament segments can be calculated from Equation 2.28 and Equation 2.30. The temperature is set as $T = 300K$, and the energy will be measured in k_BT unit. The cross-link spring constant k is set as $0.25pN/\mu m \approx 60k_BT/\mu m^2$, with a rest length $a_c = 0.05\mu m$ and a maximum allowed extension $a_m = 0.25\mu m$. The mass of a cross-link protein molecule is chosen as $1.05 \times 10^5 amu \approx 1.74 \times 10^{-22} kg$, therefore, the *thermal de Broglie wavelength* λ_B of a cross-link is $3.1 \times 10^{-7} \mu m$. The chemical binding energy ε_b between both ends of a cross-link and two filaments is set as $10kcal/mol$ and the concentration of gas phase cross-links c is set to be $1 \times 10^5 \mu m^{-3}$. The cross-linking rate parameter ν_0 is set to be $10^{-3} s^{-1}$. Since the network with unconstrained filaments can hardly reach equilibrium and the average cross-link lifetime varies at non-equilibrium states, we will measure the system time in 'second' instead of τ_0 in this chapter. The steric interactions between filaments were not considered in the simulation, so that the filaments can get any closer or pass each other.

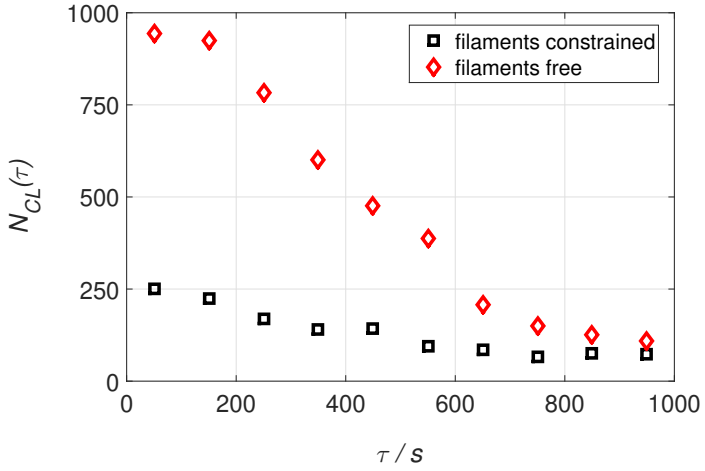

Figure 4.2: Histogram of cross-link lifetime for filament-constrained network (black squares) and bundling network with free filaments (red diamonds). Both networks are controlled to evolve for $1000s$ from the initial state, and the histogram interval is $100s$.

4.3 Results

4.3.1 Formation of bundles

The formation of bundles due to cross-linking is observed in the network. The homogeneous and isotropic configuration of filaments at initial state, as shown in Figure 4.1 (a), turns into a configuration of filament bundles, as shown in Figure 4.1 (b). The filaments in the same bundle are densely cross-linked, while the filaments belong to different bundles are rarely cross-linked except at the connections between bundles.

During the formation of bundles, an enhanced cross-linking dynamics is observed comparing with the control group, where both networks evolve for the same amount of time. As one can imagine, a newly formed cross-link in the filament fluid will bring the corresponding filaments closer, which breaks the homogeneousness of the network and results in an increase in the number of candidate binding sites for lower-elastic energy cross-links. The local binding rates of the gas phase cross-links among these sites are also enhanced and this process continues as a chain reaction, where the cross-links serve as catalysts for themselves. If

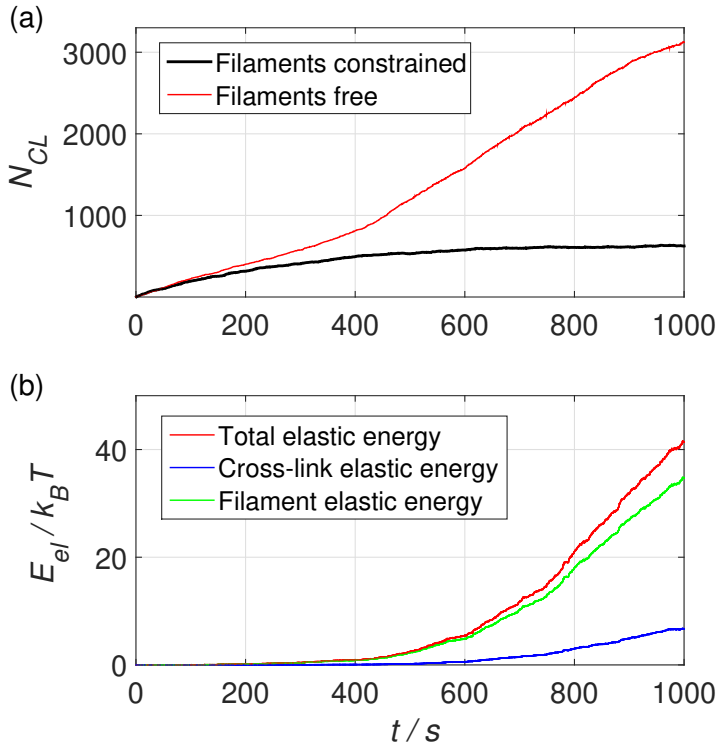

Figure 4.3: (a) Number of bound cross-links change over time for filament-constrained network (black) and bundling network with free filaments (red). (b) Total elastic energy of the bundling network (red), the elastic energy stored in cross-links (blue), and the elastic energy stored in filaments (green).

two filaments are cross-linked by more than two linkers, they are more likely to be parallel, which gradually shapes the filament islands into bundles. The enhanced binding rates in the bundles give birth to a large number of bound cross-links, whose overall unbinding rate also keep increasing in order to reach an equilibrium state of the current configuration, but they never succeed since the equilibrium is always shifting further due to more bundling. Figure 4.2 shows the histogram of cross-link lifetime for the network with free filaments (red diamonds) and the control group with constrained filaments (black squares), and we observe a greater number of ever existed cross-links in the former network at each lifetime interval, especially for the short-lived cross-links, indicating an enhanced cross-linking dynamics in the bundling network.

As discussed in Chapter 3, the cross-link lifetime for the control group with constrained filaments follows an exponential distribution, and the average cross-link lifetime in this case is $380s$. Surprisingly, the average cross-link lifetime for the network with bundles is shortened rather than prolonged due to the enhanced cross-linking rates, which is $310s$ in this case. This against-physical-intuition observation can be explained in term of the limitation of the KMC method: First, only one cross-linking event is allowed to happen during a specific time interval in the KMC method, while the cross-linking can occur simultaneously everywhere in real networks, which assists holding the network structure and controls the growth of cross-linking rates. Second, the KMC method selects one cross-linking event among all possibilities at a given state, which results in affects from other cross-linking events on this one, while in real systems the bond breaking is spontaneous and is only determined by the tensile force on the bond itself. From the KMC algorithm, the lifetime of a cross-link q formed at i-th step can be written as

$$\tau^q = \Delta t_i + (1 - P^q_{i+1,off})\Delta t_{i+1} + (1 - P^q_{i+1,off})(1 - P^q_{i+2,off})\Delta t_{i+2} + \cdots , \qquad (4.1)$$

where $P^q_{i,off} = \frac{\nu^q_{i,off}}{\nu_{i,tot}}$ is the probability that the breaking event of cross-link q at step i is selected among all possibilities with its unbinding rate $\nu^q_{i,off}$ and a total cross-linking rate $\nu_{i,tot}$, and $\Delta t_i = -\frac{\ln \zeta_i}{\nu_{i,tot}}$ is the system time spent on i-th step with a uniformly distributed random number $\zeta_i \in (0, 1]$. At the beginning stage of bundle formation, the cross-link shortens its stretching length the moment it is formed, resulting in a decreasing $\nu^q_{i+1,off}$ at the next step, but the change of the total rate $\nu_{i+1,tot}$ is hard to determine since now it becomes a competition between the dramatically reduced unbinding rate of this cross-link and an increasing total binding rate, resulting from a higher binding rate at each possible site and an increasing number of these high-rate candidate sites. At the stage when enough filaments are in the bundles, the newly born cross-links within the bundle cannot shorten their stretching length dramatically due to the constraints from other cross-links in the bundle. Therefore, their unbinding rates $\nu^q_{i+1,off}$ and the total rate $\nu_{i+1,tot}$ are basically stable, which tends to maintain their lifetimes. From the observation, the overall effect of these mechanisms is a shortened average cross-link lifetime, mainly due to the fast growing total cross-linking rate.

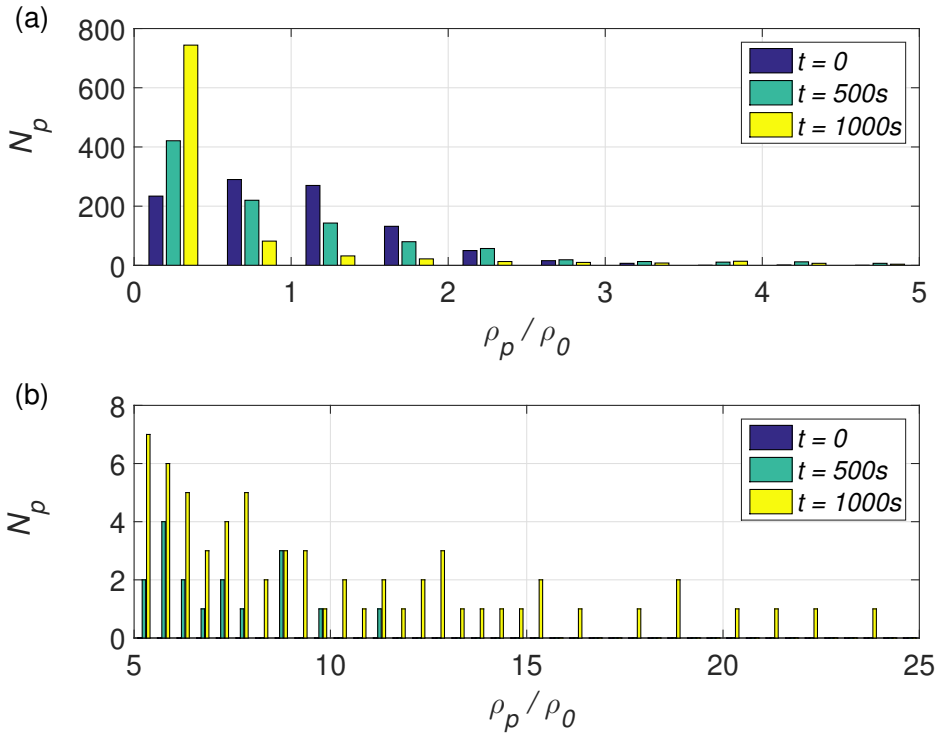

Figure 4.4: Histogram of the (filament length) density of pixels ρ_p measured in the average density ρ_0 unit at $t = 0$(purple), $t = 500s$(green) and $t = 1000s$(yellow). (a) Data of interval $\rho_p/\rho_0 \in (0, 5]$. (b) Data of interval $\rho_p/\rho_0 \in (5, 25]$. The histogram interval is 0.5 and the vertical axis is the number of pixels N_p, which are measured in different magnitudes in part (a) and (b).

4.3.2 Bundle growth

The enhanced cross-linking dynamics in the bundles cumulatively results in a large number of intrabundle cross-links, as shown in Figure 4.3 (a) and Figure 4.1 (b). The number of bound cross-links in the control group of filaments constrained network stabilizes at around 650, while this number keeps growing in the bundling network due to the increasing density of bundles, leading to over 3000 bound cross-links at $t = 1000s$. However, the intrabundle cross-links are slightly stretched, and the elastic energy of the network are mainly stored in the filaments, as shown in Figure 4.3 (b). The equilibrium elastic energy of the control group is one magnitude higher than the bundling network, which is not shown in the plot,

and the average cross-link energy of the control group is ~ 250 times greater than the value of the bundling network.

In general, the bundles provide high-density breeding grounds for low-energy cross-links with high cross-linking rates, and the system tends to condense more gas phase cross-links to recover an instant equilibrium state. However, this instant equilibrium keeps shifting over time towards a direction that requires a higher number of bound cross-links, and the condensing process is always chasing behind. The cumulative effect is a monotonically increasing number of bound cross-links over time.

To explore the dynamics of bundle growth, we evenly divide the $10\mu m \times 10\mu m \times 10\mu m$ box into a large number of small sub-boxes, which can be treated as three-dimensional pixels of the box. The (filament length) density in each pixel can be measured through finding the ratio of the total filament length in the pixel and the volume of the pixel. The average (filament length) density of the entire network ρ_0 can be expressed as

$$\rho_0 = \frac{N\ell}{V}, \tag{4.2}$$

where N is the total number of filaments in the network, ℓ is the length of each filament, and V is the volume of the box. In this case, $\rho_0 = 2\mu m^{-2}$. Suppose the box is divided into N_0 equal-volume cubic pixels, the (filament length) density of a pixel ρ_p can be expressed as

$$\rho_p = \frac{\sum_{pixel} \ell_{pixel}}{\frac{V}{N_0}} = \frac{\sum_{pixel} \ell_{pixel}}{v}, \tag{4.3}$$

where $\sum_{pixel} \ell_{pixel}$ is the total length of filaments confined in the pixel and $v = \frac{V}{N_0}$ is the volume of a pixel. At the initial state, ρ_p should roughly follow a Poisson distribution with the average number $\lambda = \rho_0$. Noticing that the variables in a Poisson distribution can only take integers, this length density measurement is equivalent to counting the number of tiny filament segments, where ρ_0 can be defined as the average number of filament segments in a pixel for the entire network and ρ_p is defined as the total number of filament segments confined in a pixel. Due to the equivalency of these two measurements, in this chapter, we will stick to the density measuring for more accuracy and ρ_p will be normalized by ρ_0 from now on.

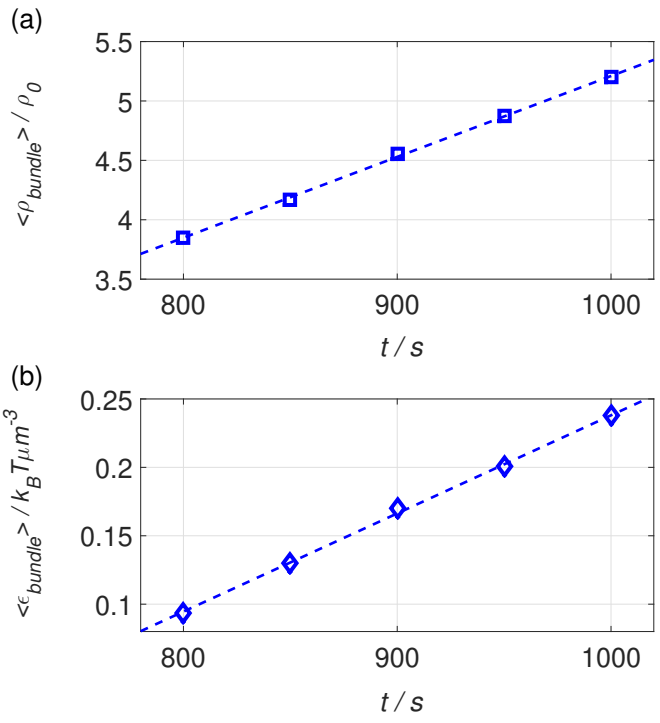

Figure 4.5: Bundle growth over time. (a) Average (filament length) density of bundles $< \boldsymbol{\rho}_{bundle} >$ normalized by ρ_0 against time, with data point (squares) and a linear function fitting curve (dashed line) of $< \boldsymbol{\rho}_{bundle} > /\rho_0 \approx 0.0068t/s - 1.60$. (b) Average energy density of bundles $< \boldsymbol{\epsilon}_{bundle} >$ against time, with data points (diamonds) and a linear function fitting curve (dashed line) of $< \boldsymbol{\epsilon}_{bundle} > /(k_B T \mu m^{-3}) \approx 0.00072t/s - 0.48$.

During the process of bundle formation, we observe a polarization in the distribution of ρ_p/ρ_0 over time, as shown in Figure 4.4, where both the number of low-density (or empty) pixels and high-density pixels increase over time. This indicates a gradually broken homogeneousness over time, as expected, where the filaments tend to condense at a small volume with an increasing local density and leave a growing number of pixels empty.

The elastic energy of the bundling network continuously increases instead of stabilizing at an equilibrium value as we observed in the filament-constrained networks, as shown Figure 4.3 (b). We find this energy growth over time is directly related to the bundle growth in density, especially in the time-domain of $800s \sim 1000s$, where the elastic energy grows rapidly and linearly. We made a simple assumption to locate the pixels of bundles: If the pixel density ρ_p

is greater than ρ_0, we treat this pixel as a part of a bundle and will call it a 'bundle pixel'; If ρ_p is smaller than ρ_0, we then treat this pixel as a part of the cavity and will call it a 'cavity pixel'. The average (filament length) density of bundles in the entire network $< \boldsymbol{\rho}_{bundle} >$ can then be written as

$$< \boldsymbol{\rho}_{bundle} >= \frac{\sum_{bundle}(\rho_p v)}{V_{bundle}} = \frac{1}{N_{bundle}} \sum_{bundle} \rho_p =< \rho_p >_{bundle}, \tag{4.4}$$

where the volume of the bundles V_{bundle} is expressed by the product of the number of bundle pixels N_{bundle} and the pixel volume v as $V_{bundle} = N_{bundle}v$. Surprisingly, we find the average density of bundles $< \boldsymbol{\rho}_{bundle} >$ grows almost linearly over time between $t = 800s$ and $t = 1000s$, as shown in Figure 4.5 (a), resulting from a combination of facts that more filaments join the bundles and the bundles volumetrically shrink slightly. On the other hand, the average elastic energy density of the bundles can be approximated as

$$< \boldsymbol{\epsilon}_{bundle} >\approx \frac{E_{el}}{V_{bundle}}, \tag{4.5}$$

where we have assumed all the elastic energy contribution is from the bundles as $E_{bundle} \approx E_{el}$, which is highly acceptable since the cavities store almost zero elastic energy. We find the $< \boldsymbol{\epsilon}_{bundle} >$ also grows linearly over time between $t = 800s$ and $t = 1000s$, as shown in Figure 4.5 (b). Inspiringly, we find both growth rates of the average density and the average energy density of bundles are constant in this time-domain, which leads to a linear relation between these two densities as

$$\frac{\partial < \boldsymbol{\epsilon}_{bundle} >}{\partial < \boldsymbol{\rho}_{bundle} >} = \frac{\partial E_{bundle}}{\partial L_{bundle}} = K, \tag{4.6}$$

where E_{bundle} is the total energy of the bundle, L_{bundle} is the total length of filaments in the bundle, and the proportionality constant K has a dimension of $force$ ($energy/length$) in this case, which physically describes the average contribution from per unit length growth of bundled filaments to the bundle energy increase. Interestingly, this contribution constant is not only time-irrelevant, but also independent of the density of the bundle at the current state.

In general, the bundle growth dynamics can be understood in terms of the following: At the beginning stage, the cross-links keep condensing the filaments into bundles, resulting in

an enhanced cross-linking dynamics and an increasing number of intrabundle cross-links; In the time-domain where the bundles grow rapidly, the density of bundles increases linearly over time, and each unit length growth of the bundled filaments on average contributes to a constant bundle elastic energy increase, which is responsible for the linear growth of the elastic energy of the network. The network can hardly reach equilibrium state since there is neither steric interactions between filaments nor outward pressure to keep the filaments apart, and we speculate the network will eventually condense into a large bundle containing all filaments.

4.4 Discussion

In this chapter, we apply the finite element kinetic Monte Carlo method to create semiflexible networks, and the bundle formation of the filaments is observed in the presence of transient cross-links. To explore the dynamics of the bundling process, we introduce a control group of the network in which the filaments are constrained, and we find the cross-linking dynamics in the bundling network is dramatically enhanced due to the catalysis of the cross-links themselves, which cumulatively results in a much greater number of intrabundle cross-links that store very low elastic energy comparing with the control group. We also find, In the time-domain where the bundles grow rapidly, the average (filament length) density of the bundles grows linearly over time, and each equal amount of length growth of the bundled filaments on average contributes to a time-independent constant bundle elastic energy growth regardless of the current density of the bundles, which causes the linearly increasing elastic energy of the network.

CHAPTER 5

Summary and Outlook

5.1 Summary of Results

In this dissertation, we propose a finite element kinetic Monte Carlo simulation method to explore the dynamics of semiflexible networks with transient cross-links. We first discuss the detailed rationales individually of the finite element treatment, kinetic Monte Carlo approach, and L-BFGS minimization method, and then come up with an integrated algorithm combining these ideas to explore the formation process and the zero-frequency dynamics of the semiflexible networks.

This simulation method is used to probe into the stress relaxation dynamics of densely linked three-dimensional filament networks with transient cross-links, where the constrained filaments in the network are sheared affinely and the stress relaxation is caused by the strain-driven cross-link reorganization. We prove the strain energy of the network scales quadratically with the strain from a theoretical approach, and we testify this theory with simulation results. We find the strain energy mainly arises from the deformation growth of highly-stretched cross-links orientating in certain directions, where both the number and the average elastic energy growth of these cross-links scale linearly with the strain. We also find the exponential dissipation of the strain energy is due to the cross-link reorganization towards the equilibrium state, and the isotropy and orientational symmetry of the bound cross-links, which were broken under the strain, are restored during the relaxation. The configuration of cross-links is trained during the stress relaxation process in a manner tending to maintain the current strain on the filaments.

When applying this simulation method to construct semiflexible networks from filament

fluid, we observe the cross-linking-driven formation of bundles in these networks. We also observe a high accumulation of intrabundle cross-links with low elastic energy due to an enhanced cross-linking dynamics in the bundles. We explore the dynamics of bundling in the time-domain where the bundles grow rapidly, and we find both the density and energy density of the bundles grow linearly over time, which leads to a linear dependence between the bundle energy growth and the bundled filament length growth. This indicates the bundle energy growth is only related to the amount of newly recruited filaments and is independent of the current bundle density.

5.2 Future Work and Outlook

There are many aspects we can improve in the simulation: First, the three-dimensional steric interactions between filaments were not considered in the current simulation, so that the filaments can get any closer or pass each other, which is not physical. We hope further developments on the simulation are able to include these interactions in three dimensions. Second, the natural formation of bundles in the network reduces the shear modulus of the network, since most cross-links are found in the bundles and the key to create a network with large shear modulus is the high quantity of the interbundle cross-links. If treating the bundles as thicker and more rigid 'filaments', the rigidity percolation transition of the network occurs when enough of these 'filaments' are connected through the 'inter-filament' cross-links, but the intrabundle spots are much more attractive to the gas phase cross-links. We attempted to create a network with a large shear modulus in various ways, such as introducing scaffolding filaments, attaching/breaking cross-links in stages by tuning their stiffness, and artificially cross-linking filaments at the initial state, however, none of them achieves the expectation at this point. We encourage our intelligent peers to develop better methods for making networks with large enough shear moduli. Third, since the L-BFGS optimization method is dealing with a extremely large number of variables, in some occasions it fails to determine the optimal search direction in this high-dimensional variable space, especially when highly-stretched cross-links form/break or a large strain is applied to the network. We expect

a new integrated method, combining the high-efficient KMC/L-BFGS algorithm and the dependable Brownian dynamics(BD) simulation, can make a difference. Just like the hybrid QM/MM(quantum mechanics/molecular mechanics) approach for multi-scale molecule-level simulations[79], the KMC/L-BFGS accounts for speed, and the BD accounts for accuracy, especially when L-BFGS optimization fails.

At the same time, we expect verifications on these theories and simulation results from related experiments. First, we will suggest a zero-frequency strain controlled shear experiment on densely cross-linked networks with rigid filaments, in which the cross-linking molecules are recommended to have s softer stiffness (which provides a wider distribution of their stretching lengths). The strained controlled shear can be applied to the network by attaching or gluing two plates to the top and bottom surfaces of the network and moving them to the opposite directions. Through measuring the forces on the plates that needed to shear the network and hold the strain, we can acquire the stress. The linear elasticity of the network can be tested through varying the strain and checking the stress(right after shear)-strain curve. Similarly, the stress relaxation data can be acquired by measuring the time-dependent forces needed to maintain the current offset of the plates(which maintains the current strain). If we hold the sheared plates for a long enough time until the stress decays to zero (or a minimum value), by removing the plates and measuring the deformation change of the network, we can verify the training effects on the network. Second, we suggest preforming experiments on the formation stage of the networks. The naive idea is to mix the solutions of cross-links and biopolymers and observe the evolution of the biopolymers. We can estimate the volume of the bundles from the fluorescence spectroscopy of the network from different angles and estimate the mass of the bundles by subtracting the amount of free biopolymers from the total amount in the original solution. The bundle growth dynamics can then be pictured from the time evolution of the estimated density of the bundles. Certainly, these immature experimental designs are nothing but armchair strategies without detailed validations and improvements from the creative experimentalists in the field.

REFERENCES

[1] Gijsje H. Koenderink, Zvonimir Dogic, Fumihiko Nakamura, Poul M. Bendix, Frederick C. MacKintosh, John H. Hartwig, Thomas P. Stossel, and David A. Weitz. An active biopolymer network controlled by molecular motors. *Proceedings of the National Academy of Sciences*, 106(36):15192–15197, 2009.

[2] F. C. MacKintosh, J. Käs, and P. A. Janmey. Elasticity of semiflexible biopolymer networks. *Phys. Rev. Lett.*, 75:4425–4428, Dec 1995.

[3] B. A. DiDonna and Alex J. Levine. Unfolding cross-linkers as rheology regulators in f-actin networks. *Phys. Rev. E*, 75:041909, Apr 2007.

[4] Qi Wen and Paul A. Janmey. Polymer physics of the cytoskeleton. *Current Opinion in Solid State and Materials Science*, 15(5):177 – 182, 2011.

[5] C. P. Broedersz and F. C. MacKintosh. Modeling semiflexible polymer networks. *Rev. Mod. Phys.*, 86:995–1036, Jul 2014.

[6] Fumihiko Nakamura, Teresia M. Osborn, Christopher A. Hartemink, John H. Hartwig, and Thomas P. Stossel. Structural basis of filamin a functions. *The Journal of Cell Biology*, 179(5):1011–1025, 2007.

[7] Sabyasachi Rakshit, Yunxiang Zhang, Kristine Manibog, Omer Shafraz, and Sanjeevi Sivasankar. Ideal, catch, and slip bonds in cadherin adhesion. *Proceedings of the National Academy of Sciences*, 109(46):18815–18820, 2012.

[8] David A. Head, Alex J. Levine, and F. C. MacKintosh. Deformation of cross-linked semiflexible polymer networks. *Phys. Rev. Lett.*, 91:108102, Sep 2003.

[9] D. A. Head, A. J. Levine, and F. C. MacKintosh. Distinct regimes of elastic response and deformation modes of cross-linked cytoskeletal and semiflexible polymer networks. *Phys. Rev. E*, 68:061907, Dec 2003.

[10] M. L. Gardel, J. H. Shin, F. C. MacKintosh, L. Mahadevan, P. Matsudaira, and D. A. Weitz. Elastic behavior of cross-linked and bundled actin networks. *Science*, 304(5675):1301–1305, 2004.

[11] G. E. Pike and C. H. Seager. Percolation and conductivity: A computer study. i. *Phys. Rev. B*, 10:1421–1434, Aug 1974.

[12] Jan Wilhelm and Erwin Frey. Elasticity of stiff polymer networks. *Phys. Rev. Lett.*, 91:108103, Sep 2003.

[13] M. Latva-Kokko and J. Timonen. Rigidity of random networks of stiff fibers in the low-density limit. *Phys. Rev. E*, 64:066117, Nov 2001.

[14] M. Latva-Kokko, J. Mäkinen, and J. Timonen. Rigidity transition in two-dimensional random fiber networks. *Phys. Rev. E*, 63:046113, Mar 2001.

[15] J. A. Åström, J. P. Mäkinen, M. J. Alava, and J. Timonen. Elasticity of poissonian fiber networks. *Phys. Rev. E*, 61:5550–5556, May 2000.

[16] Jan strm, Sami Saarinen, Kaarlo Niskanen, and Juhani Kurkijrvi. Microscopic mechanics of fiber networks. *Journal of Applied Physics*, 75(5):2383–2392, 1994.

[17] D. A. Head, F. C. MacKintosh, and A. J. Levine. Nonuniversality of elastic exponents in random bond-bending networks. *Phys. Rev. E*, 68:025101, Aug 2003.

[18] R.L. Satcher and C.F. Dewey. Theoretical estimates of mechanical properties of the endothelial cell cytoskeleton. *Biophysical Journal*, 71(1):109 – 118, 1996.

[19] Pethrick RA. Polymer physics. edited by michael rubinstein and ralph h colby oxford university press, oxford, 2003. isbn 019852059x. pp 440. *Polymer International*, 53(9):1394–1395.

[20] Klaus Kroy and Erwin Frey. Force-extension relation and plateau modulus for wormlike chains. *Phys. Rev. Lett.*, 77:306–309, Jul 1996.

[21] Moumita Das, F. C. MacKintosh, and Alex J. Levine. Effective medium theory of semiflexible filamentous networks. *Phys. Rev. Lett.*, 99:038101, Jul 2007.

[22] Alex J Levine, D A Head, and F C MacKintosh. The deformation field in semiflexible networks. *Journal of Physics: Condensed Matter*, 16(22):S2079, 2004.

[23] Mo Bai, Andrew R. Missel, William S. Klug, and Alex J. Levine. The mechanics and affine-nonaffine transition in polydisperse semiflexible networks. *Soft Matter*, 7:907–914, 2011.

[24] B. Schnurr, F. Gittes, F. C. MacKintosh, and C. F. Schmidt. Determining microscopic viscoelasticity in flexible and semiflexible polymer networks from thermal fluctuations. *Macromolecules*, 30(25):7781–7792, 1997.

[25] G. H. Koenderink, M. Atakhorrami, F. C. MacKintosh, and C. F. Schmidt. High-frequency stress relaxation in semiflexible polymer solutions and networks. *Phys. Rev. Lett.*, 96:138307, Apr 2006.

[26] B. Hinner, M. Tempel, E. Sackmann, K. Kroy, and E. Frey. Entanglement, elasticity, and viscous relaxation of actin solutions. *Phys. Rev. Lett.*, 81:2614–2617, Sep 1998.

[27] Chase P. Broedersz, Martin Depken, Norman Y. Yao, Martin R. Pollak, David A. Weitz, and Frederick C. MacKintosh. Cross-link-governed dynamics of biopolymer networks. *Phys. Rev. Lett.*, 105:238101, Nov 2010.

[28] C Heussinger. Stress relaxation through crosslink unbinding in cytoskeletal networks. *New Journal of Physics*, 14(9):095029, 2012.

[29] F. Gittes and F. C. MacKintosh. Dynamic shear modulus of a semiflexible polymer network. *Phys. Rev. E*, 58:R1241–R1244, Aug 1998.

[30] David C. Morse. Viscoelasticity of tightly entangled solutions of semiflexible polymers. *Phys. Rev. E*, 58:R1237–R1240, Aug 1998.

[31] David C. Morse. Viscoelasticity of concentrated isotropic solutions of semiflexible polymers. 1. model and stress tensor. *Macromolecules*, 31(20):7030–7043, 1998.

[32] Sabine M. Volkmer Ward, Astrid Weins, Martin R. Pollak, and David A. Weitz. Dynamic viscoelasticity of actin cross-linked with wild-type and disease-causing mutant α-actinin-4. *Biophysical Journal*, 95(10):4915 – 4923, 2008.

[33] D.H. Wachsstock, W.H. Schwarz, and T.D. Pollard. Cross-linker dynamics determine the mechanical properties of actin gels. *Biophysical Journal*, 66(3, Part 1):801 – 809, 1994.

[34] Daisuke Mizuno, Catherine Tardin, C. F. Schmidt, and F. C. MacKintosh. Nonequilibrium mechanics of active cytoskeletal networks. *Science*, 315(5810):370–373, 2007.

[35] Kei W. Müller, Robijn F. Bruinsma, Oliver Lieleg, Andreas R. Bausch, Wolfgang A. Wall, and Alex J. Levine. Rheology of semiflexible bundle networks with transient linkers. *Phys. Rev. Lett.*, 112:238102, Jun 2014.

[36] O. Lieleg, M. M. A. E. Claessens, C. Heussinger, E. Frey, and A. R. Bausch. Mechanics of bundled semiflexible polymer networks. *Phys. Rev. Lett.*, 99:088102, Aug 2007.

[37] Oliver Lieleg, Jürgen Kayser, Gianfranco Brambilla, Luca Cipelletti, and Alexandra R Bausch. Slow dynamics and internal stress relaxation in bundled cytoskeletal networks. *Nature materials*, 10 3:236–42, 2011.

[38] Yali Yang, Mo Bai, William S. Klug, Alex J. Levine, and Megan T. Valentine. Microrheology of highly crosslinked microtubule networks is dominated by force-induced crosslinker unbinding. *Soft Matter*, 9:383–393, 2013.

[39] Christian Vaca, Roie Shlomovitz, Yali Yang, Megan T. Valentine, and Alex J. Levine. Bond breaking dynamics in semiflexible networks under load. *Soft Matter*, 11:4899–4911, 2015.

[40] GI Bell. Models for the specific adhesion of cells to cells. *Science*, 200(4342):618–627, 1978.

[41] Louis Foucard and Franck J. Vernerey. A thermodynamical model for stress-fiber organization in contractile cells. *Applied Physics Letters*, 100(1):013702, 2012.

[42] Andrew R. Missel, Mo Bai, William S. Klug, and Alex J. Levine. Affine-nonaffine transition in networks of nematically ordered semiflexible polymers. *Phys. Rev. E*, 82:041907, Oct 2010.

[43] LC Foucard, JK Price, WS Klug, and AJ Levine. Cooperative buckling and the nonlinear mechanics of nematic semiflexible networks. *Nonlinearity*, 28(9):R89, 2015.

[44] Sayantan Majumdar, Louis Foucard, Alex J. Levine, and Margaret L. Gardel. Encoding mechano-memories in actin networks. 2017(Unpublished).

[45] M. Dembo, D. C. Torney, K. Saxman, and D. Hammer. The reaction-limited kinetics of membrane-to-surface adhesion and detachment. *Proceedings of the Royal Society of London. Series B, Biological Sciences*, 234(1274):55–83, 1988.

[46] Bryan T Marshall, Mian Long, James W Piper, Tadayuki Yago, Rodger P McEver, and Cheng Zhu. Direct observation of catch bonds involving cell-adhesion molecules. 423:190–3, 06 2003.

[47] Kristine Manibog, Hui Li, Sabyasachi Rakshit, and Sanjeevi Sivasankar. Resolving the molecular mechanism of cadherin catch bond formation. 5:3941, 06 2014.

[48] Erik Finger, Kamal Puri, Ronen Alon, Michael Lawrence, Ulrich H. von Andrian, and Timothy Springer. Adhesion through l-selectin requires a threshold hydrodynamic shear. 379:266–9, 02 1996.

[49] J. T. Bullerjahn and K. Kroy. Analytical catch-slip bond model for arbitrary forces and loading rates. *Phys. Rev. E*, 93:012404, Jan 2016.

[50] O. Lieleg, K.M. Schmoller, M.M.A.E. Claessens, and A.R. Bausch. Cytoskeletal polymer networks: Viscoelastic properties are determined by the microscopic interaction potential of cross-links. *Biophysical Journal*, 96(11):4725 – 4732, 2009.

[51] Melanie Norstrom and Margaret L. Gardel. Shear thickening of f-actin networks crosslinked with non-muscle myosin iib. *Soft Matter*, 7:3228–3233, 2011.

[52] Norman Y. Yao, Chase P. Broedersz, Martin Depken, Daniel J. Becker, Martin R. Pollak, Frederick C. MacKintosh, and David A. Weitz. Stress-enhanced gelation: A dynamic nonlinearity of elasticity. *Phys. Rev. Lett.*, 110:018103, Jan 2013.

[53] A. W. C. Lau, B. D. Hoffman, A. Davies, J. C. Crocker, and T. C. Lubensky. Microrheology, stress fluctuations, and active behavior of living cells. *Phys. Rev. Lett.*, 91:198101, Nov 2003.

[54] Linhong Deng, Xavier Trepat, James Butler, Emil Millet, Kathleen Morgan, David A Weitz, and Jeffrey Fredberg. Fast and slow dynamics of the cytoskeleton. 5:636–40, 09 2006.

[55] Alex J. Levine and F. C. MacKintosh. The mechanics and fluctuation spectrum of active gels. *The Journal of Physical Chemistry B*, 113(12):3820–3830, 2009.

[56] W M Young and E W Elcock. Monte carlo studies of vacancy migration in binary ordered alloys: I. *Proceedings of the Physical Society*, 89(3):735, 1966.

[57] A.B. Bortz, M.H. Kalos, and J.L. Lebowitz. A new algorithm for monte carlo simulation of ising spin systems. *Journal of Computational Physics*, 17(1):10 – 18, 1975.

[58] Kristen A. Fichthorn and W. H. Weinberg. Theoretical foundations of dynamical monte carlo simulations. *The Journal of Chemical Physics*, 95(2):1090–1096, 1991.

[59] Arthur F Voter. Introduction to the kinetic monte carlo method. *Radiation effects in solids*, pages 1–23, 2007.

[60] C.J. Cyron and W.A. Wall. Numerical method for the simulation of the brownian dynamics of rodlike microstructures with threedimensional nonlinear beam elements. *International Journal for Numerical Methods in Engineering*, 90(8):955–987, 2012.

[61] Christian J. Cyron, Kei W. Mller, Andreas R. Bausch, and Wolfgang A. Wall. Micromechanical simulations of biopolymer networks with finite elements. *Journal of Computational Physics*, 244:236 – 251, 2013.

[62] C. G. BROYDEN. The convergence of a class of double-rank minimization algorithms 1. general considerations. *IMA Journal of Applied Mathematics*, 6(1):76–90, 1970.

[63] R. Fletcher. A new approach to variable metric algorithms. *The Computer Journal*, 13(3):317–322, 1970.

[64] Donald Goldfarb. A family of variable-metric methods derived by variational means. *Mathematics of Computation*, 24(109):23–26, 1970.

[65] D. F. Shanno. Conditioning of quasi-newton methods for function minimization. *Mathematics of Computation*, 24(111):647–656, 1970.

[66] Jorge Nocedal. Updating quasi-newton matrices with limited storage. *Mathematics of Computation*, 35:773–782, 7 1980.

[67] Richard H. Byrd, Jorge Nocedal, and Robert B. Schnabel. Representations of quasi-newton matrices and their use in limited memory methods. *Mathematical Programming*, 63(1):129–156, Jan 1994.

[68] R. Byrd, P. Lu, J. Nocedal, and C. Zhu. A limited memory algorithm for bound constrained optimization. *SIAM Journal on Scientific Computing*, 16(5):1190–1208, 1995.

[69] Ciyou Zhu, Richard H Byrd, Peihuang Lu, and Jorge Nocedal. Algorithm 778: L-bfgs-b: Fortran subroutines for large-scale bound-constrained optimization. *ACM Transactions on Mathematical Software (TOMS)*, 23(4):550–560, 1997.

[70] Jack Sherman and Winifred J. Morrison. Adjustment of an inverse matrix corresponding to a change in one element of a given matrix. *The Annals of Mathematical Statistics*, 21(1):124–127, 1950.

[71] W. S. Klug et. al. Variational object-oriented mechanics.

[72] A. W. Lees and S. F. Edwards. The computer study of transport processes under extreme conditions. *Journal of Physics C: Solid State Physics*, 5(15):1921, 1972.

[73] A. N. Kolmogorov. Sulla Determinazione Empirica di una Legge di Distribuzione. *Giornale dell'Istituto Italiano degli Attuari*, 4:83–91, 1933.

[74] N. Smirnov. Table for estimating the goodness of fit of empirical distributions. *Ann. Math. Statist.*, 19(2):279–281, 06 1948.

[75] J. H. Shin, M. L. Gardel, L. Mahadevan, P. Matsudaira, and D. A. Weitz. Relating microstructure to rheology of a bundled and cross-linked f-actin network in vitro. *Proceedings of the National Academy of Sciences*, 101(26):9636–9641, 2004.

[76] Anja Schmidt and Michael N. Hall. Signaling to the actin cytoskeleton. *Annual Review of Cell and Developmental Biology*, 14(1):305–338, 1998.

[77] Andras Kis, G Csnyi, Jean-Paul Salvetat, Thien-Nga Lee, E Couteau, Andrzej Kulik, W Benoit, Juergen Brugger, and L Forr. Reinforcement of single-walled carbon nanotube bundles by intertube bridging. *Nature materials*, 3:153–7, 04 2004.

[78] Francesco Pampaloni, Gianluca Lattanzi, Alexandr Jonáš, Thomas Surrey, Erwin Frey, and Ernst-Ludwig Florin. Thermal fluctuations of grafted microtubules provide evidence of a length-dependent persistence length. *Proceedings of the National Academy of Sciences*, 103(27):10248–10253, 2006.

[79] A. Warshel and M. Levitt. Theoretical studies of enzymic reactions: Dielectric, electrostatic and steric stabilization of the carbonium ion in the reaction of lysozyme. *Journal of Molecular Biology*, 103(2):227 – 249, 1976.